

Sobhani, A., Saeedifar, M., Najafabadi, M. A., Fotouhi, M. and Zarouchas, D. (2018)
The study of buckling and post-buckling behavior of laminated composites consisting
multiple delaminations using acoustic emission. *Thin-Walled Structures*, 127, pp. 145-
156.

There may be differences between this version and the published version. You are
advised to consult the publisher's version if you wish to cite from it.

<http://eprints.gla.ac.uk/196772/>

Deposited on: 19 September 2019

The Study of Buckling and Post-Buckling Behavior of Laminated Composites Consisting Multiple Delaminations Using Acoustic Emission

Anvar Sobhani¹, Milad Saeedifar^{1,2}, Mehdi Ahmadi Najafabadi^{*1}, Mohamad Fotouhi³,
Dimitrios Zarouchas²

1. Non-destructive Testing Lab, Department of Mechanical Engineering, Amirkabir University of Technology, 424 Hafez Ave, 15914, Tehran, Iran.
2. Structural Integrity & Composites Group, Faculty of Aerospace Engineering, Delft University of Technology, The Netherlands.
3. Department of Design and Mathematics, University of the West of England, Bristol BS16 1QY, UK.

Abstract

This study introduces a comprehensive set of designed and tested glass/epoxy composites, AE monitoring and signal processing techniques; (i) to investigate the effect of multiple delaminations on buckling and post-buckling behaviors of laminated composites and (ii) to evaluate Acoustic Emission (AE) technique ability to monitor the buckling delamination growth and to classify the occurred damage mechanisms. The pre-delaminations were made by inserting a Teflon film at the plies interfaces during fabrication. Three different types of specimens were fabricated and subjected to compression loading to study the effects of the location, the number of delaminations, and the thickness of the Teflon film on buckling and post-buckling behaviors of the specimens. The mechanical results showed that the number of delaminations has a major effect on the critical and maximum loads and the location of delamination and the thickness of the Teflon film have minor effects on the critical and maximum loads. The AE signals of the specimens were then classified using Gaussian Mixture Model (GMM) and the evolution of different damage mechanisms was investigated. The AE results showed that AE is a robust technique to classify damage mechanisms in buckling of laminated composites and could identify delamination propagation earlier and with a lower standard deviation, compared with the conventional methods.

^{*} Corresponding author. Tel.: +98 21 6454 3431; fax: +98 21 8871 2838. E-mail address: ahmadin@aut.ac.ir (M. Ahmadi Najafabadi)

Keywords: Buckling; Post-buckling; Multiple Delamination; Laminated Composites; Acoustic Emission.

1. Introduction

Fiber Reinforced Polymer (FRP) composites are utilized increasingly in many industries due to their high specific strength and stiffness [1-3]. Despite their advantages, these materials suffer from different damage mechanisms such as matrix cracking, fiber breakage, and delamination [4-6]. Delamination is the most common damage mode in laminated composites that significantly reduces the stiffness of the structure [4]. Delamination is particularly critical when the structure is subjected to in-plane compressive loading. In this situation, complex interactions between buckling, post-buckling, and delamination evolution can occur [7].

Delamination usually occurs at the interior layers of laminated composites, thus it is not visible to the eye from the outside. In order to detect delamination in composite structures, different Non-Destructive Evaluation (NDE) methods have been used [8-11]. Among the NDE techniques, Acoustic Emissions (AE) have a good applicability for in-situ monitoring [12-15].

Some researchers have investigated the buckling and post-buckling behavior of laminated composites consisting of one or multiple delaminations using experimental, analytical and numerical methods [16-19]. Hosseini Toudeshky et al. [20] studied the effect of composite lay-ups on the delamination propagation in specimens under in-plane compression loading. They showed that delamination propagation could be controlled by changing the composite's lay-up. They also stated that delamination propagation rate decreased by increasing the vertical displacement of the specimen. Gu and Chattopadhyay [21] investigated the effects of the location and the length of delamination on buckling and post-buckling behavior of carbon/epoxy composite plates using

analytical and experimental methods. The results showed that the buckling mode was closely dependent on the location and length of the delamination.

In recent years, some research has been conducted to investigate the behavior of delamination in laminated composites under tensile, mode I, mode II and mixed-mode I&II loading conditions using AE method [22-27]. Saeedifar et al. [22] predicted the propagation of delamination in glass/epoxy specimens under mode I loading using AE cumulative energy parameter. Some researchers used AE technique to classify different damage mechanisms in laminated composites under in-plane compression loading. Mohammadi et al. [25] classified different damage mechanisms in Open Hole Tensile (OHT) composite specimens under compression load. They quantified different damage mechanisms by analyzing the AE signals with wavelet transform and fuzzy clustering methods. However, as the manufactured specimens were unidirectional lay-up $([0]_{10})$ delamination did not occur. McCrory et al. [28] classified damage mechanisms in carbon/epoxy composite plates without any pre-delamination under in-plane compression loading. They classified damages in the specimens by three methods: Artificial Neural Network (ANN), Unsupervised Waveform Clustering (UWC), and Measured Amplitude Ratio (MAR). Debski et al. [29] determined the buckling load of a thin-walled carbon/epoxy channel using experiments and Finite Element Method (FEM). They utilized AE energy parameter to determine the initiation of buckling, without further analysis of the AE data. Zhou et al [30], studied the state of damage during buckling of delaminated composites using Digital Image Correlation (DIC) and AE techniques. They investigated the global state of damage, but no discriminating and detailed attention were done regarding the damage evolution and the occurred damage types such as delamination, matrix cracking and fiber breakage separately.

Based on the literature review, it was discovered that there is a lack in comprehensive AE-based study of buckling and post-buckling behavior of the delaminated composites. Therefore, the main

objective of this study is to utilize AE to investigate buckling and post-buckling behavior of glass/epoxy laminated composites with multiple pre-delaminations. To this aim, three different types of specimens, with and without pre-delaminations and with different numbers and locations of the delaminations were subjected to in-plane compression loading and the tests were monitored by AE technique. The mechanical results showed that the number of delaminations has a major effect on the critical and maximum loads and the location of delamination and the thickness of the Teflon film have minor effects on the critical and maximum loads. The AE signals of the specimens were then classified using Gaussian Mixture Model (GMM) and the evolution of different damage mechanisms was investigated. The AE technique is able to identify the propagation of delamination and the type of damage in laminated composites under in-plane compression loading and it can be used to investigate the integrity of composite structures.

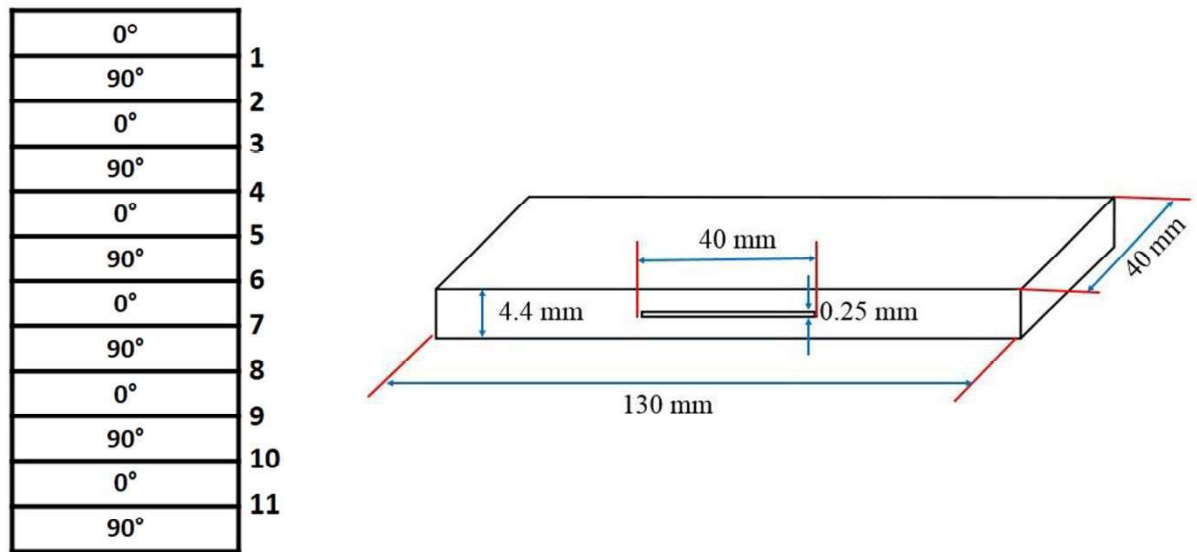
2. Experimental Procedures

2.1. Description of the Materials

The specimens were fabricated from epoxy resin EPL1012, which was mixed with EPH112 hardener and reinforced with E-glass unidirectional fibers with density of 1.17 g/cm^3 and 400 g/m^2 , respectively. The laminates were prepared by Vacuum Infusion Process (VIP) method. Inserting a Teflon film at the interface of different plies during manufacturing was used to create the artificial delaminations. The specification of the specimens is represented in Table 1 and Fig. 1.

Table 1. The specifications of the specimens.

Specimens	Delamination location	The thickness of Teflon film that serves as the artificial delamination (μm)	Lay-ups
S_P	Without pre-delamination	-	$[0^\circ / 90^\circ]_6$
S_2	2 nd interface	250	$[0^\circ / 90^\circ]_6$
S_4	4 th interface	250	$[0^\circ / 90^\circ]_6$
S_6	6 th interface	250	$[0^\circ / 90^\circ]_6$
S_{M-K}	2 nd , 4 th , and 6 th interfaces	250	$[0^\circ / 90^\circ]_6$
S_{M-N}	2 nd , 4 th , and 6 th interfaces	150	$[0^\circ / 90^\circ]_6$

**Fig. 1. The schematic of the specimens.**

2.2. Test Method

As illustrated in Figure 2, the specimens were subjected to compression loading. Compression loading was applied at a constant feed rate of 0.5 mm/min in displacement control mode and at a

temperature of 25°C. The applied load and the vertical displacement were continuously recorded during all the tests by a universal compression/tensile machine (DARTEC). The load cell capacity was 50,000 N with 10 N resolution.

In addition, the lateral deflection of the specimen was recorded by two digital dial indicators with resolution of 0.01 mm, located at the left and right sides of the specimen. In order to record the AE signals, two AE sensors were placed on the specimen surface at a distance of 40 mm from the specimen center. The test process was monitored using a digital video camera. Three coupons of each type of specimen were tested to check the tests repeatability.

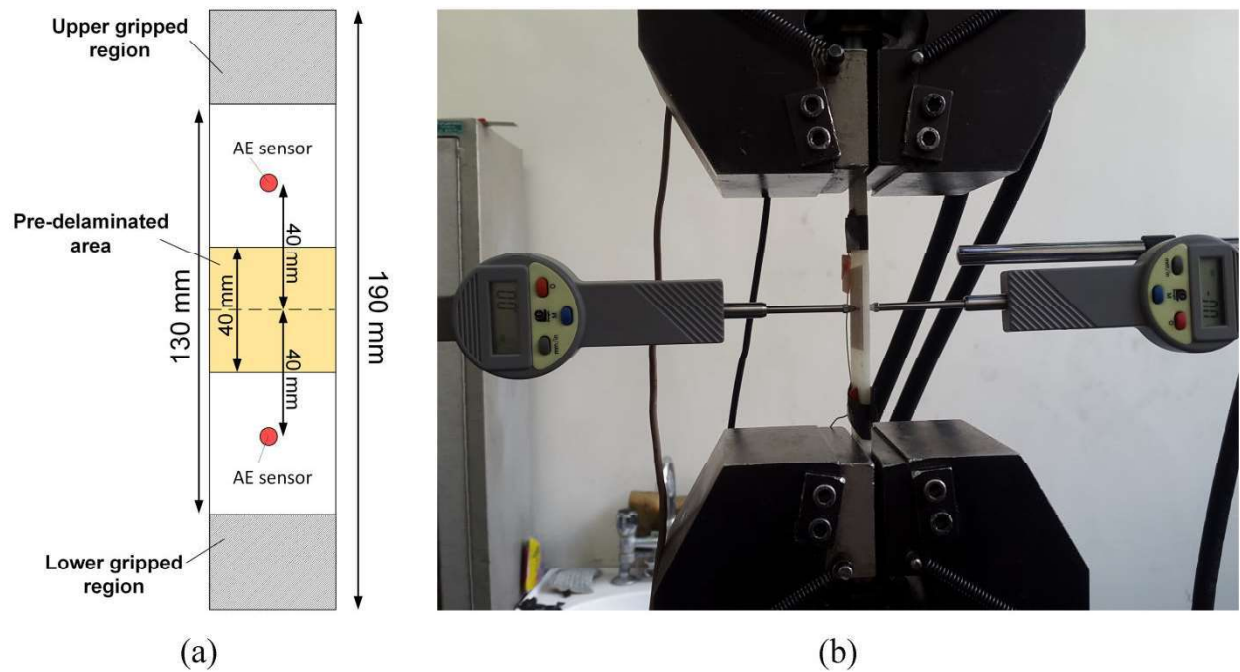


Fig 2. a) The schematic and b) the real test setup.

2.3. AE system

PICO which is a single-crystal piezoelectric transducer, from Physical Acoustics Corporation (PAC) was used as the AE sensor. It is a broadband, and resonant-type sensor with the resonance frequency and optimum operating frequency range of 513.28 kHz and [100–750 kHz],

respectively. The AE events were recorded by the AEWin software and a data acquisition system PAC-PCI-2, with a maximum sampling rate of 40 MHz. Vacuumed silicon grease was used as acoustical coupling. The recorded AE signals were enhanced by a 2/4/6-AST preamplifier. The gain selector of the preamplifier was set to 40 dB. The threshold of receiving AE signals was adjusted to 35 dB. The test-sampling rate was 1 MHz with 16 bits of resolution between 10 and 100 dB. A pencil lead break procedure was used to calibrate the data acquisition system for each specimen.

3. Gaussian Mixture Model (GMM) Clustering

Discrimination of AE events due to different types of damage in composite materials is a major problem. GMM is a probabilistic model that assumes the data are a weighted sum of a finite number of Gaussian densities with unknown parameters [31]:

$$p(x) = \sum_{k=1}^K w_k g(A|\mu_k, \Sigma_k) \quad (1)$$

$$g(A|\mu_k, \Sigma_k) = \frac{1}{\sqrt{(2\pi)^k |\Sigma_k|}} \exp\left(-\frac{1}{2} \frac{(A - \mu_k)^T}{\Sigma_k (A - \mu_k)}\right) \quad (2)$$

$$\sum_{k=1}^K w_k = 1 \quad (3)$$

where A is data, w_k is the mixture weight function, and g is the Gaussian density function with mean vector μ_k and covariance matrix Σ_k .

The GMM algorithm consists of three steps [31]:

1. The algorithm starts with some initial estimation for mean vectors and covariance matrixes. Then, it calculates the weight function for all data and all mixture combinations.

2. Using the membership weight and the data to calculate the new parameters. If the sum of membership weight for k^{th} component is defined as $N_k = \sum w_{ik}$, the new mixture weight can be calculated by:

$$w_k^{\text{new}} = \frac{N_k}{N}; \quad 1 \leq k \leq K \quad (4)$$

The new mean vector and covariance matrix for Gaussian distributions are updated as follows:

$$\mu_k^{\text{new}} = \left(\frac{1}{N_k} \right) \sum_{i=1}^n w_{ik} \cdot A_i; \quad 1 \leq k \leq K \quad (5)$$

$$\Sigma_k^{\text{new}} = \left(\frac{1}{N_k} \right) \sum_{i=1}^n w_{ik} \cdot (A_i - \mu_k^{\text{new}})(A_i - \mu_k^{\text{new}})^T; \quad 1 \leq k \leq K \quad (6)$$

3. Repeating steps 1 and 2 to satisfying the stopping criterion.

4. Results and Discussions

The obtained results are presented in two sections: the first section is dedicated to the mechanical results, and the second section is devoted to the AE results.

4.1. Mechanical Results

The compression load vs. vertical displacement curve of specimens S_p is shown in Fig. 3. The curve can be divided into three regions: I) Elastic increasing region; where there is a linear relationship between the load and displacement. In this region, no buckling occurs. II) Nonlinear increasing region; at the beginning of this region, the specimen buckles. Thus, there is a nonlinear relationship between the load and displacement. The amount of nonlinearity is small at first, but it increases with the load. III) Load descending region: at the maximum load, the specimen cannot withstand anymore load. Therefore, the load decreases gradually by increasing the vertical displacement.

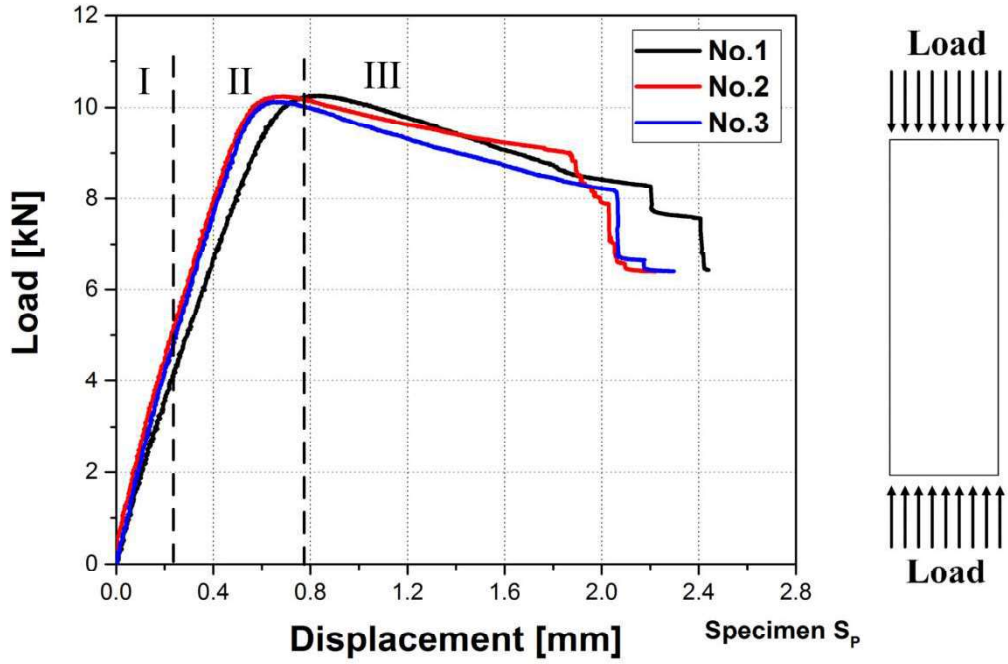


Fig. 3. The compression load vs. vertical displacement curve of specimens S_p .

Fig. 4 shows load-displacement curves of the specimens with one delamination (i.e. S_2 , S_4 , and S_6 specimens). The load-displacement curve of these specimens can be divided into three regions similar to specimen S_p . However, the nonlinear increasing region of the load curves for these specimens is greater than specimen S_p , due to local buckling. By comparing the curves of specimens S_2 , S_4 , and S_6 , it appears that when the artificial delamination is closer to the specimen's surface: 1) the load decreases faster after the maximum load (region III), and 2) the displacement corresponding to the final failure of the specimen reduces. This is due to this fact when the artificial delamination is closer to the specimen's surface, the thickness of the sub-laminate reduces, that results in local buckling of the sub-laminate at the lower loads. After this local buckling, delamination propagates and consequently the load-carrying capacity of the base-laminate diminishes. Thus, the final failure of the specimen occurs earlier.

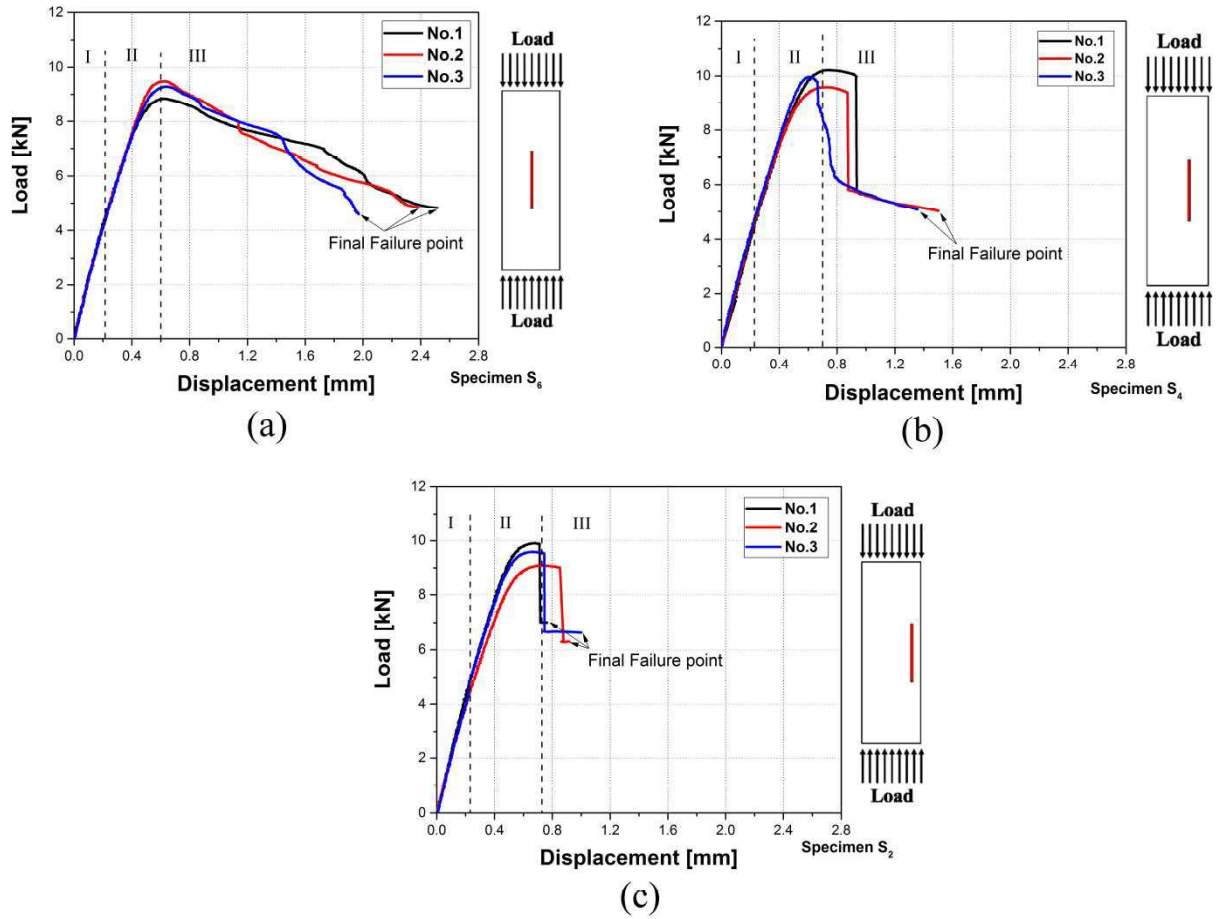


Fig. 4. The compression load vs. vertical displacement curve of specimens a) S_6 , b) S_4 , and c) S_2 .

As illustrated in Fig. 5, for specimens S_{M-K} and S_{M-N} there is a linear relationship between the load and displacement until almost load 3 kN. At this point global buckling occurs but the lateral deflection of the specimens is less than the lateral deflection of the specimens with one delamination. In the end of region I, the exterior delamination (i.e. 2nd) propagates and local buckling occurs, which is due to the lower thickness of the sub-laminate for the 2nd delamination compared with the 4th and 6th delaminations. In region II, the load-increasing rate decreases gradually until the maximum load. At this moment, the delamination 4th starts growing and the load drops instantaneously. In region III, the load-increasing rate is less than regions I and II. At the end of this region, the delamination 6th grows and the load decreases continuously. Fig. 6

shows the side view of specimen S_{M-K} in different stages of delaminations propagation. A mixed-mode buckling behavior (i.e. global and local buckling simultaneously) can be seen in this figure.

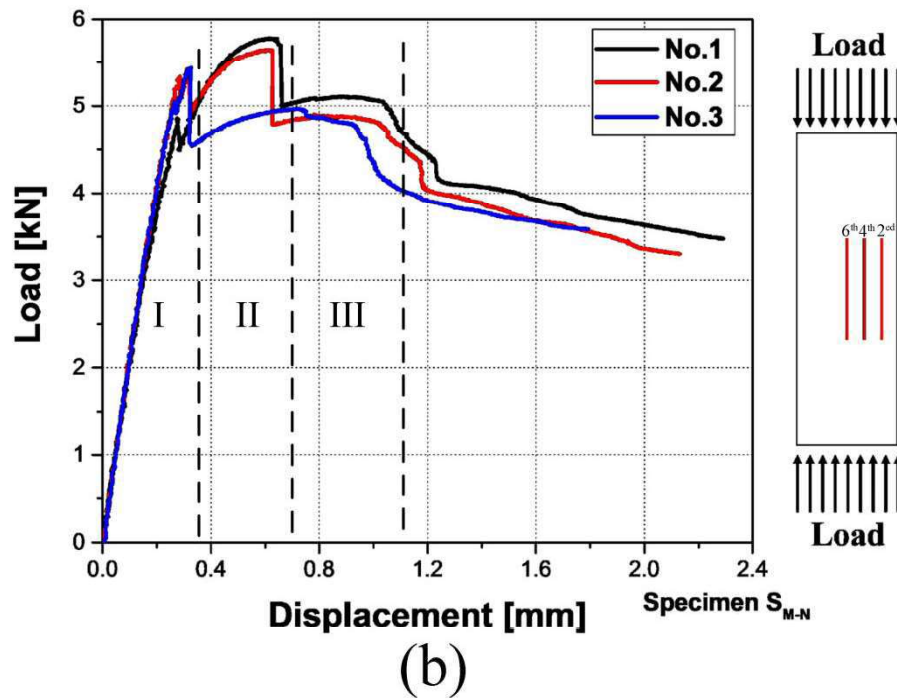
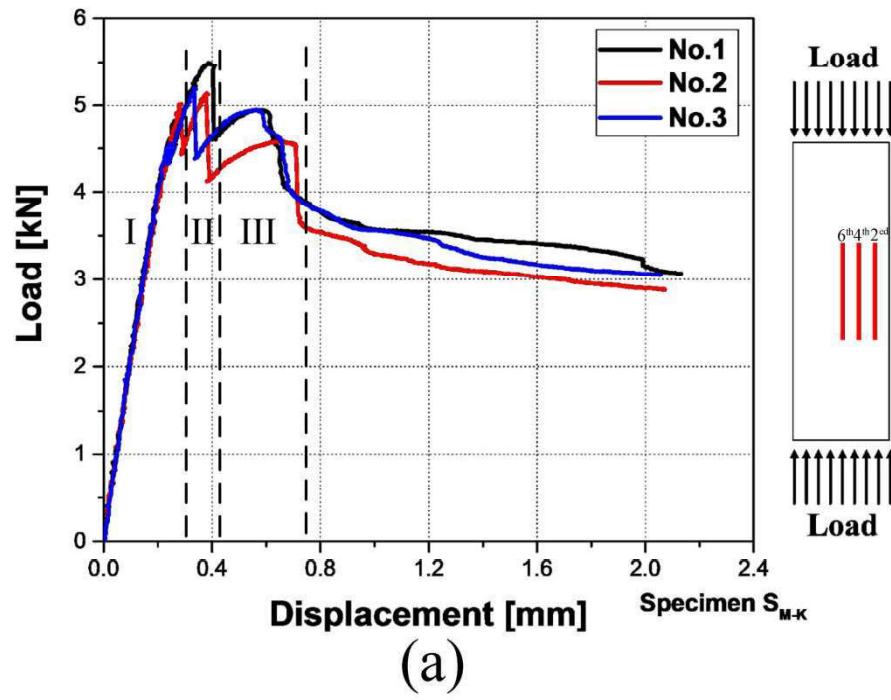


Fig 5. The compression load vs. vertical displacement curve of specimens a) S_{M-K} and b) S_{M-N} .

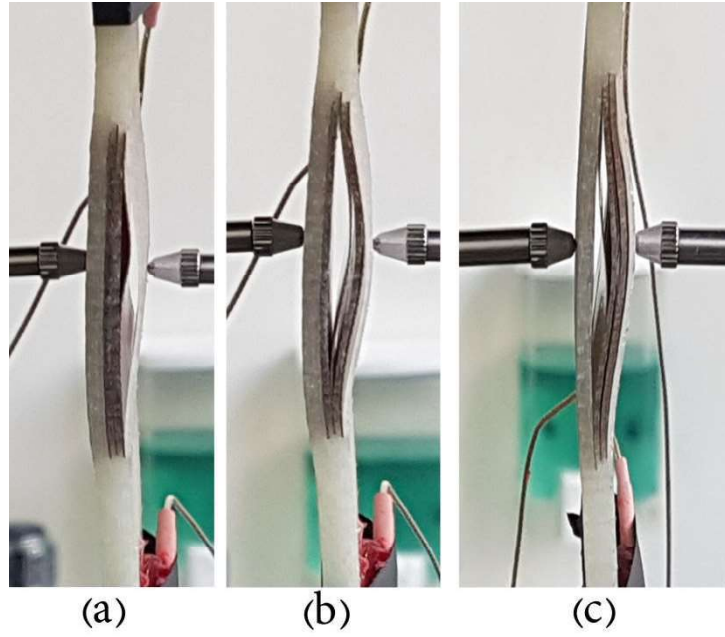


Fig. 6. The growth of a) first, b) second, and c) third delamination in specimen S_{M-K} .

Fig.7 shows load vs. lateral deflection of the specimens. The lateral deflection was recorded by two digital dial indicators. As can be seen, no lateral deflection is observed until point 1. Point 1 corresponds to the global buckling of the specimens. The lateral deflection is increased until point 2 that corresponds to the delamination induced local buckling. At this point the delamination propagates and consequently the base-laminate and the sub-laminate split from each other. Therefore, the lateral deflection curves of the base-laminate and the sub-laminate are separated. In the case of specimens S_{M-K} and S_{M-N} , after global buckling at point 1, local buckling due to propagation of the 2nd delamination is occurred at point 2. Thus, the lateral deflection curves of the base-laminate and the sub-laminate have been separated. Points 4 and 6 correspond to the growth of the 4th and 6th delaminations, respectively.

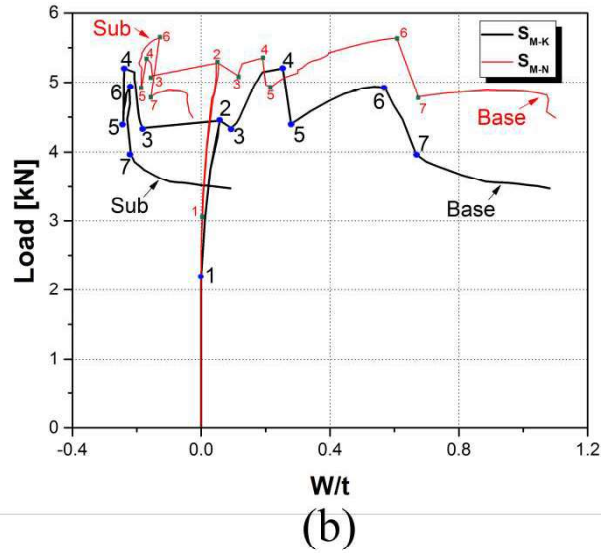
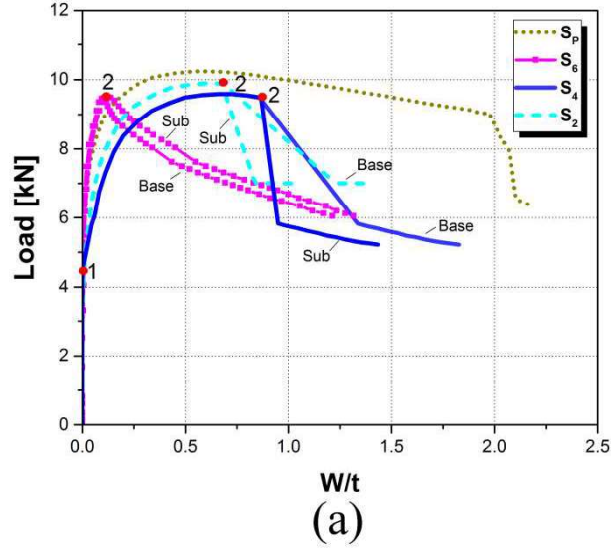


Fig. 7. Load vs. normalized lateral deflection (lateral deflection divided to the specimen's thickness) curve of the specimens a) S_P , S_2 , S_4 , and S_6 , and b) S_{M-K} , and S_{M-N} . (Base-laminate which is denoted by “Base” is the thicker part of the specimen at the side of delamination and sub-laminate which is denoted by “Sub” is the slender part of the specimen at the other side of delamination).

The effects of the location and number of delaminations and the thickness of the Teflon film that serves role of the artificial delamination on the critical buckling load and maximum load are represented in Table 2 and Fig. 8. Comparing the critical and maximum loads of specimens S_2 , S_4 , and S_6 shows that the critical and maximum loads of specimen S_4 are slightly higher than the other specimens, which is in consistent with the literature [32, 33]. As the delamination moves from the

surface (2nd interface) to the inner of the composite laminate (4th interface), stiffness of the sub-laminate increases and it leads to increasing of the buckling load, while with more growing of delamination depth from the 4th to 6th interface, stiffness of the base-laminate deteriorates and the buckling loads reduce consequently [33]. The number of delaminations has a major effect on the critical and maximum loads. The critical and maximum loads of the specimens are reduced by 47% with increasing the number of delaminations from 1 to 3 (S_2 , S_4 and S_6 compared with S_{M-K} and S_{M-N}). The comparison of the loads of specimens S_{M-K} and S_{M-N} shows that by increasing the thickness of the Teflon film, the critical and maximum loads are decreased about 6% and 5%, respectively. This is due to the increase in the thickness of the Teflon film that reduces the effective thickness of the laminate, so the global buckling occurs at the lower loads.

Table 2. The effects of the number and the location of delamination on critical buckling load and maximum load of the specimens.

Specimen	Sample No.	P_{cr}	P_{Max}	Mean of P_{cr}	Mean of P_{Max}	$\frac{P_{cr}}{P_{Max}}$	$\frac{P_{cr-i}}{P_{cr-S_p}}$	$\frac{P_{Max-i}}{P_{Max-S_p}}$
S_p	Sample 1	5.15	10.24	5.23	10.21	0.51	1	1
	Sample 2	5.21	10.26					
	Sample 3	5.32	10.13					
S_2	Sample 1	4.30	9.91	4.24	9.53	0.44	0.81	0.93
	Sample 2	4.11	9.09					
	Sample 3	4.31	9.60					
S_4	Sample 1	4.56	9.59	4.52	9.93	0.45	0.86	0.97
	Sample 2	4.58	9.97					
	Sample 3	4.42	10.22					
S_6	Sample 1	4.21	9.49	4.23	9.21	0.46	0.81	0.90
	Sample 2	4.21	9.29					
	Sample 3	4.27	8.85					
S_{M-K}	Sample 1	2.94	5.13	2.93	5.27	0.56	0.56	0.52
	Sample 2	2.93	5.49					
	Sample 3	2.93	5.20					
S_{M-N}	Sample 1	3.00	5.65	3.12	5.62	0.56	0.60	0.55
	Sample 2	3.22	5.78					
	Sample 3	3.14	5.43					

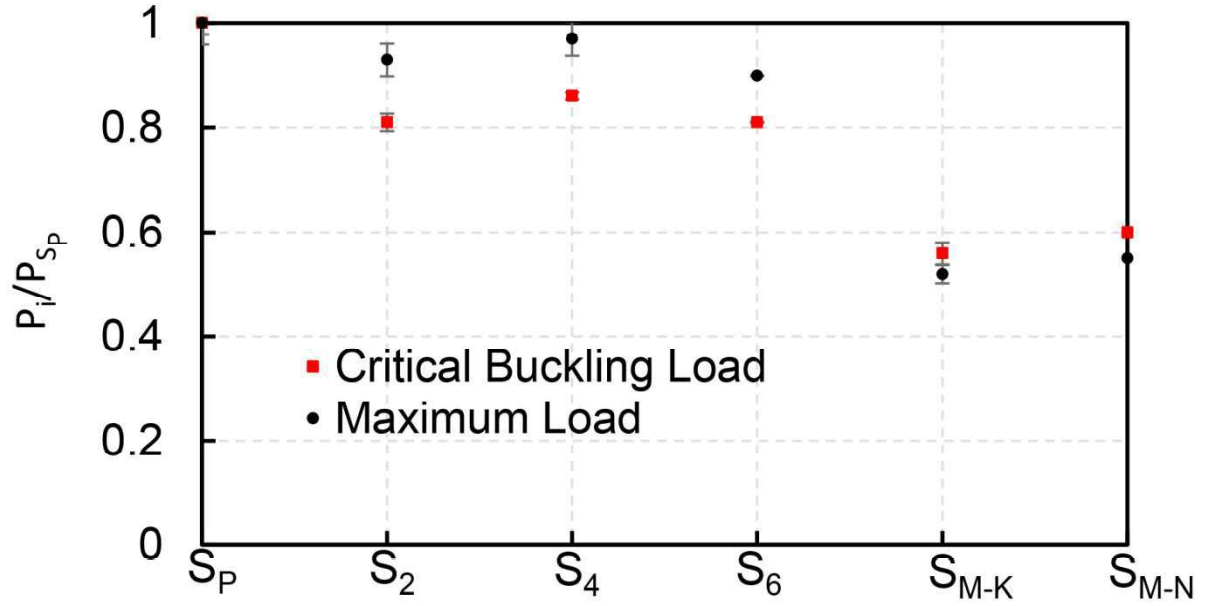


Fig. 8. The ratio of the critical and maximum loads of the specimens to the critical and maximum loads of specimen S_P with the standard deviation.

4.2. AE results

Due to good repeatability of the tests, only one curve for each type of specimens is presented in the following figures, to avoid complexity in the graphs. Fig. 9 shows the load, AE energy, and cumulative AE count versus displacement curves of specimen S_4 . According to the AE energy intensity, this diagram can be divided into three sections, which are consistent with the three sections shown in Fig. 4.b. In the first section, no damage occurs, thus, no AE activity is observable. In the second section, the specimen buckles, which leads to some micro damages. Therefore, low energy AE events are observed in this section. In the third section delamination propagates instantaneously, thus high energy AE events are seen. First high energy AE event is considered as the initial growth of delamination. After the initial growth of delamination, fiber bridging occurs in the specimen, thus the rate of delamination propagation is reduced and the energy of the AE activities is decreased. Fig 9.b shows cumulative AE count diagram of

specimen S₄. The cumulative AE count diagram can also be divided into three sections; based on the slope of the curve: region I) where there is no AE event, as no damage occurs in the specimen. Region II) where the rate of cumulative AE count curve is low. It shows the occurrence of some micro damages, because macro damage mechanisms usually generate high energy signals. Region III) where the rate of cumulative AE count curve is high. At the first of this region, delamination propagates and consequently other damage mechanisms are activated in the specimen.

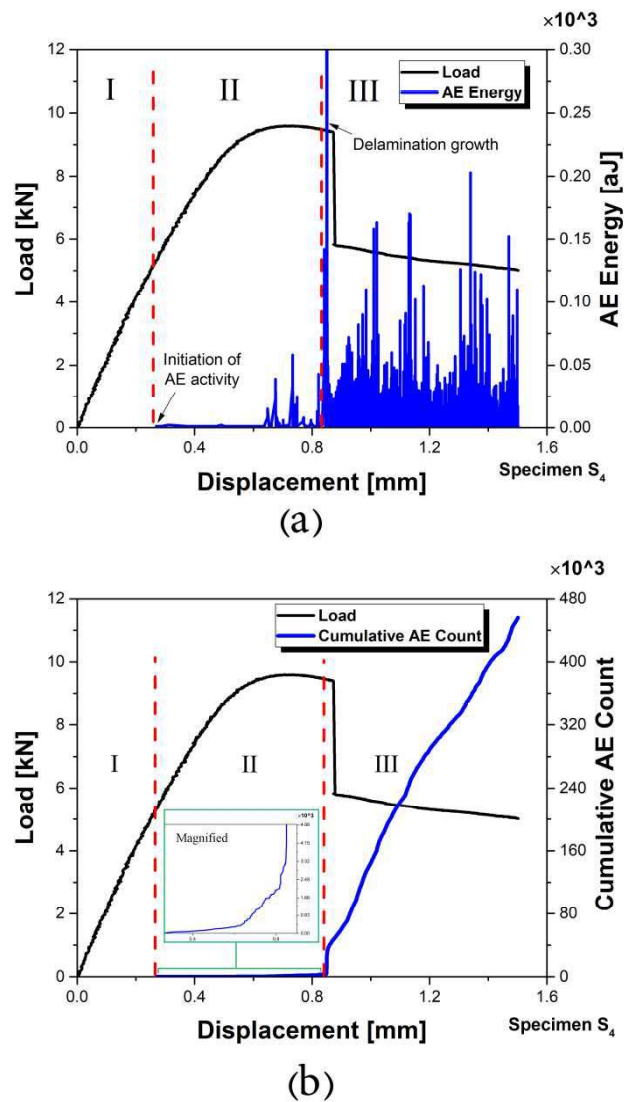


Fig. 9. a) The AE energy and b) the cumulative AE count curves of specimen S₄.

Fig. 10 shows the load, AE energy, and cumulative AE count versus displacement curves of specimen S_{M-K} . There are three burst activities and three jumps in the AE energy and cumulative AE count curves, respectively. According to Fig. 7 and the recorded videos during the tests, these jumps correspond to the growth of the three delaminations. Thus, AE can precisely identify the growth of delamination in the specimen.

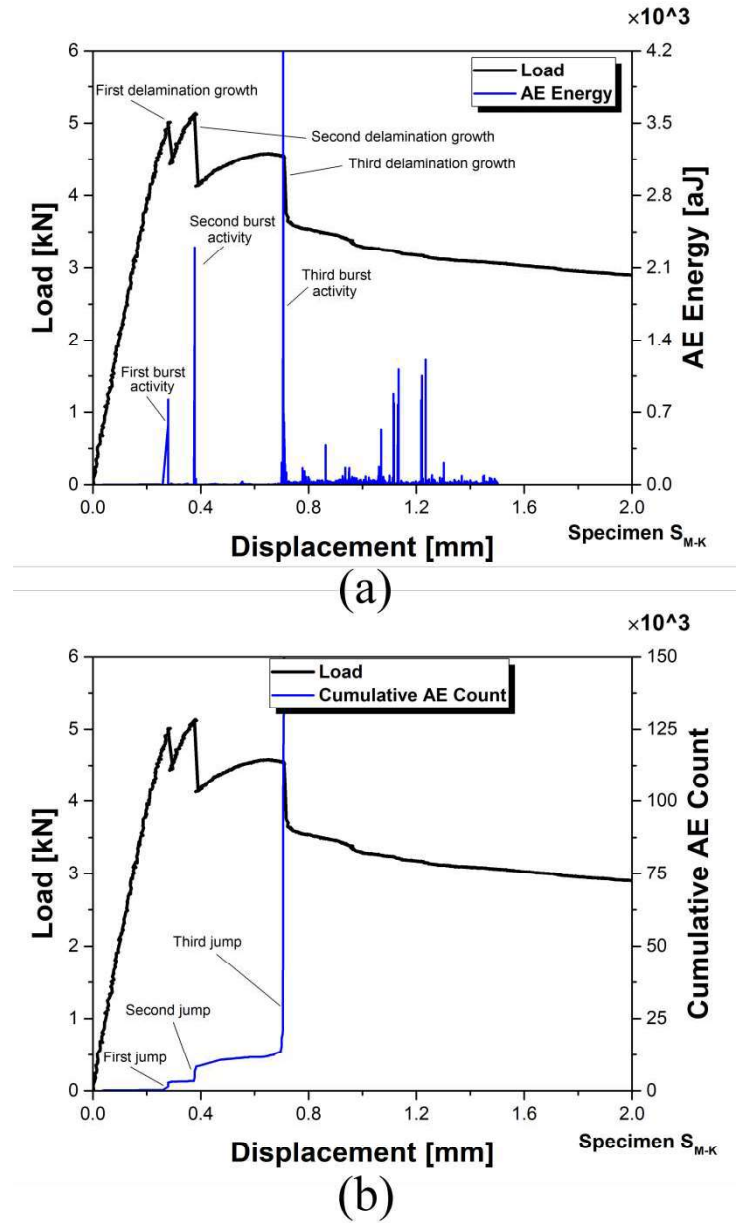


Fig. 10. a) The AE energy and b) the cumulative AE count of specimen S_{M-K} .

4.2.1. Sentry Function

Sentry function has been defined as the logarithmic ratio of the mechanical energy (area beneath the load-displacement curve) to the cumulative AE energy [34]. According to the damage status in the specimens under loading, four different trends of sentry function can be observed: I) increasing trend: this trend shows that no damage has occurred in the specimens. II) Instantaneously drop: it shows the severe damage such as delamination growth. III) Gradually decreasing: this trend indicates the microscopic damage such as matrix cracking. IV) Stable state: it shows the balancing of the mechanical damage and the AE activities.

Fig. 11 shows sentry function curves of specimens S_{M-K} and S_4 . For specimen S_{M-K} , at the beginning of the test, sentry function shows the increasing trend (type I) followed by a big fall (type II). This fall indicates growth of the 2nd delamination. After this load drop, the second type I function is observed which has lower slope compared with the first type I function. This fact shows that the specimens can still bear larger loads but the stiffness of the specimen is slightly reduced. The second and the third drops of the sentry function curve correspond to the growth of the 4th and 6th delaminations, respectively. After each drop, the slope of type I function is reduced, showing the effect of delamination growth on the stiffness reduction. For specimen S_4 , the first type II function is considered as the initial delamination growth.

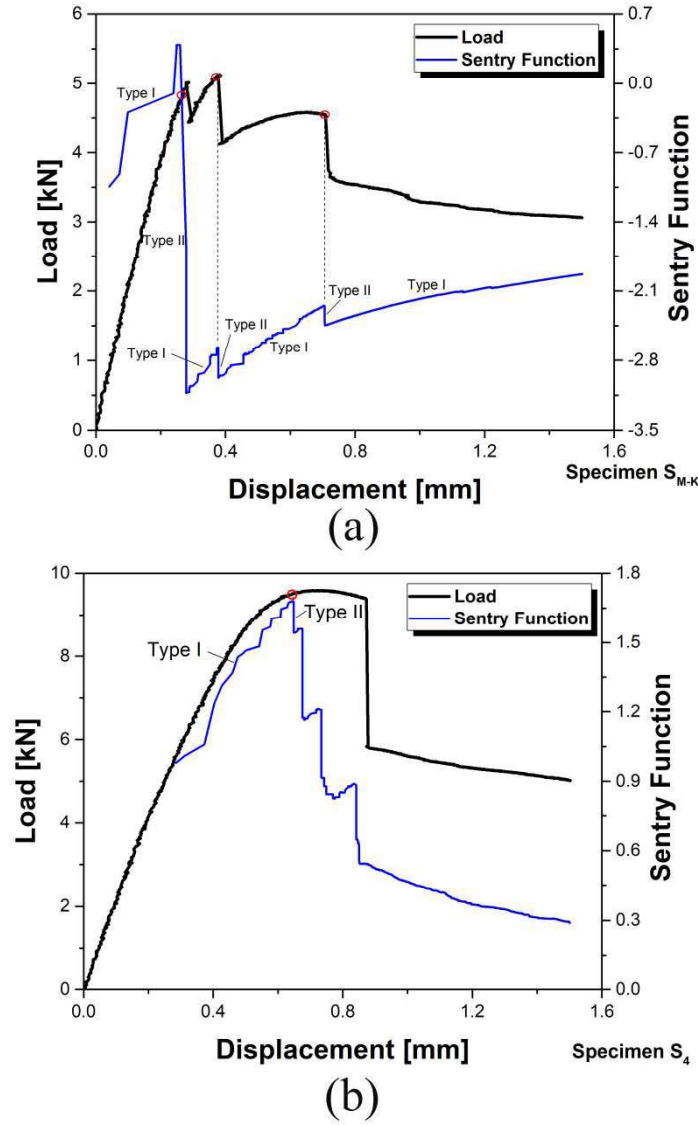


Fig. 11. The sentry function curves of specimens a) S_{M-K} and b) S_4 .

4.2.2. Classification of damage mechanisms by AE

According to literature review, the best parameters for AE signals clustering in composite materials are frequency and amplitude [35-36]. Thus these two parameters are selected as the AE features of the specimens AE signals for the clustering process. Prior to the clustering, the optimum number of clusters should be specified. To this aim, Gap criterion [37] is utilized to specify the optimum clusters number. The highest value of the Gap index shows the best clusters number. Fig.

12 shows the values of Gap index for different cluster numbers. The best clusters number according to this index is 3.

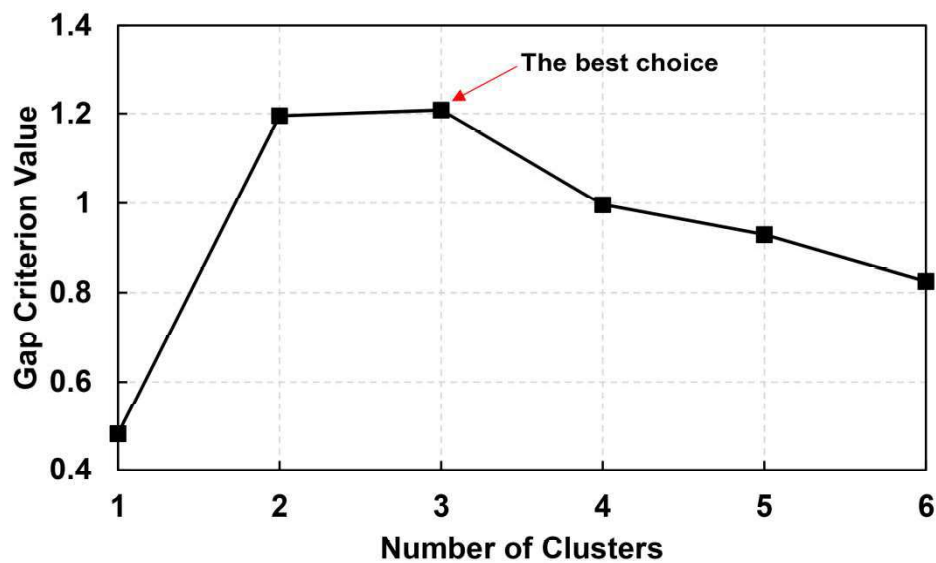


Fig. 12. The optimum clusters number for AE signals of the specimens.

The AE signals of the specimens are classified using GMM clustering method. Fig. 13 shows the clustered AE signals of the specimens. As can be seen, GMM partitioned data into three classes with approximate frequency ranges of [50-180 kHz], [180-330 kHz], and [330-500 kHz].

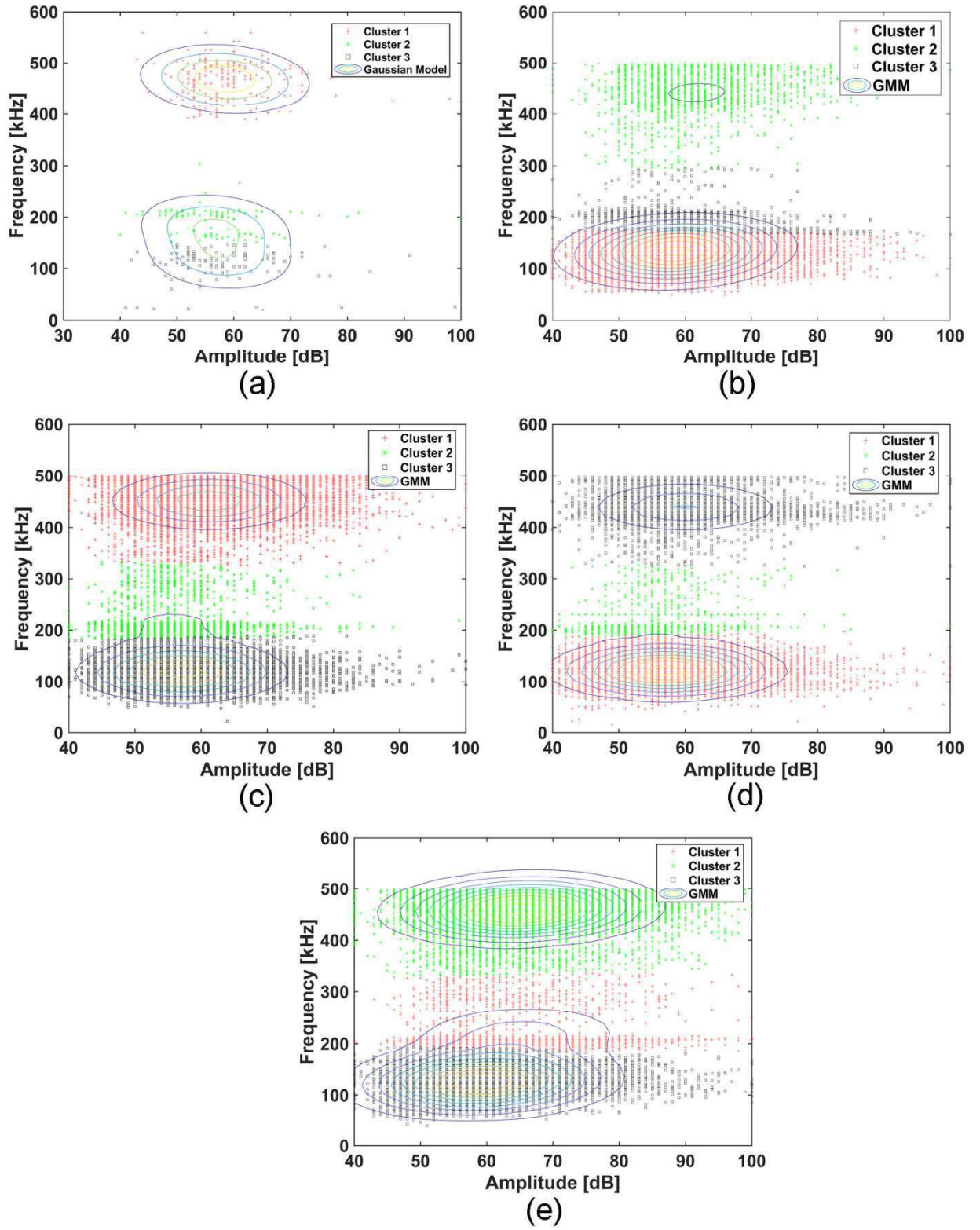


Fig. 13. The clustering of AE signals by GMM for specimens a) S₂, b) S₄, c) S₆, d) S_{M-K}, and e) S_{M-N}.

Now, the clustered data should be dedicated to the damage mechanisms. According to the previous research [38], different damage mechanisms usually have specific frequency ranges. Three main damage mechanisms in laminated composites are delamination, matrix cracking, and fiber breakage [4-6]. In our previous study [38], the frequency range of each damage mechanism was obtained by conducting some experiments such as tensile tests of pure resin and fiber bundle. The results [38] showed that the peak frequency ranges of delamination, matrix cracking, and fiber breakage are [50-170 kHz], [170-250 kHz], and [350-500 kHz], respectively (see Fig.14). Therefore, the class with the lowest frequency is dedicated to delamination, the class with the highest frequency is devoted to fiber breakage, and finally, the class with the medium frequency is allocated to matrix cracking.

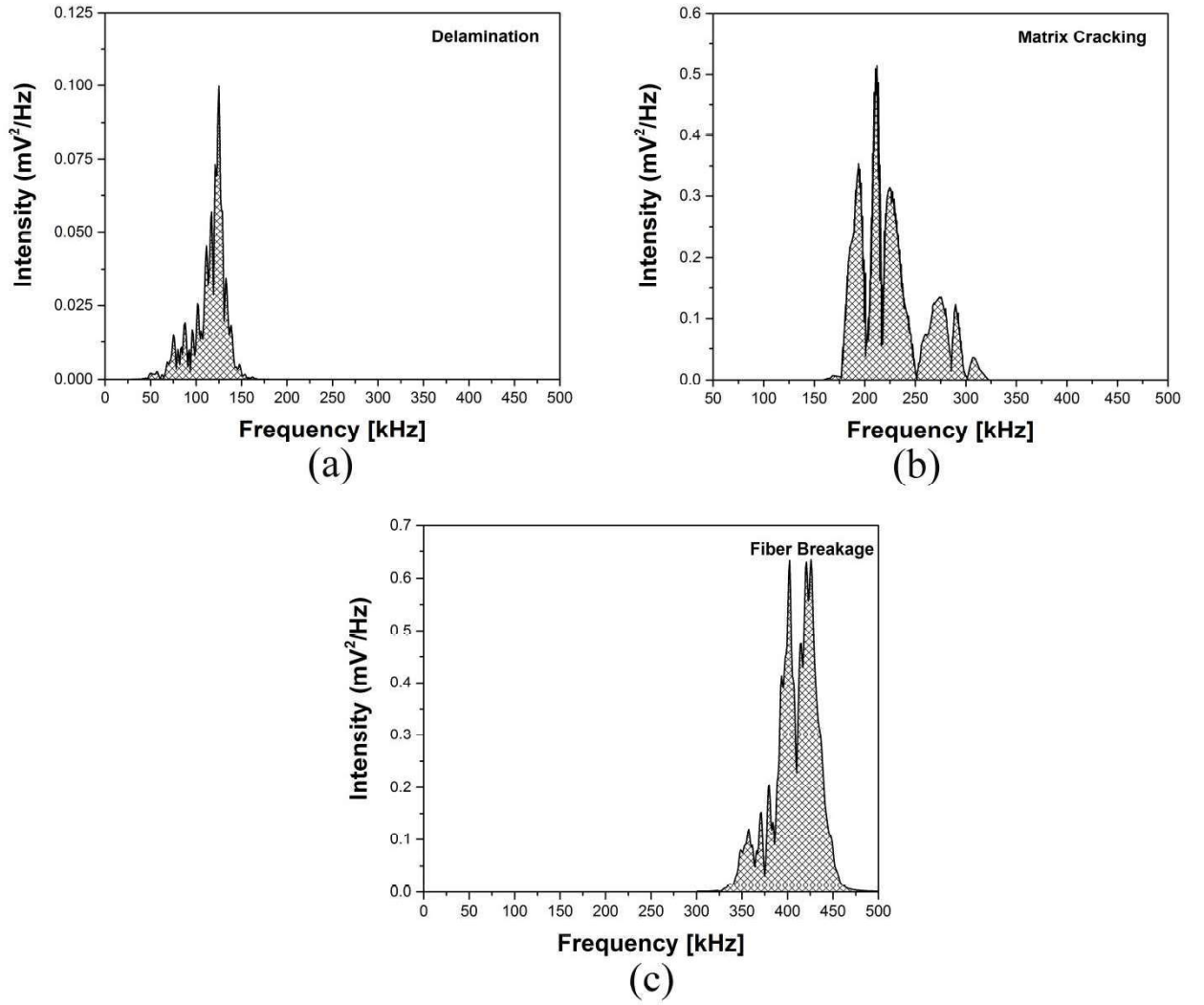


Fig. 14. The peak frequency range of the AE signals of a) delamination, b) matrix cracking, and c) fiber breakage [37].

Fig. 15 shows the cumulative AE energy of each damage mechanism. Before the delamination growth there is no considerable damage in the specimens, while by increasing of delamination signals that shows the delamination initiation, other damage mechanisms increase. In all cases, the energy curve of delamination damage could well predict the initiation of delamination. The increasing trend of the fiber breakage signals energy after the delamination growth is almost due to breakage of the bridged fibers between two adjacent plies of delamination (see Fig. 16). The localization of these signals confirms this claim. Fiber bridging controls and restrains the growth

of delamination. Comparing the cumulative AE energy curves for fiber breakage and delamination in Fig. 15 shows that both curves have a similar trend. When the cumulative curve of the fiber breakage signals is smooth, i.e. low number of fibre breakage signals, the cumulative delamination energy is low as well (except the second and third jumps in delamination energy curve of S_{M-K} and S_{M-N} specimens that are due to the initiation of new delaminations at the other interfaces). The smooth trend in the cumulative AE energy curves means that there is no significant fiber breakage and delamination growth. When the bridged fibers start failing there are sudden rises in the cumulative curves due to appearance of fiber breakage signals and at the same time the delamination grows rapidly, therefore a significant increase in the delamination energy curve is observable.

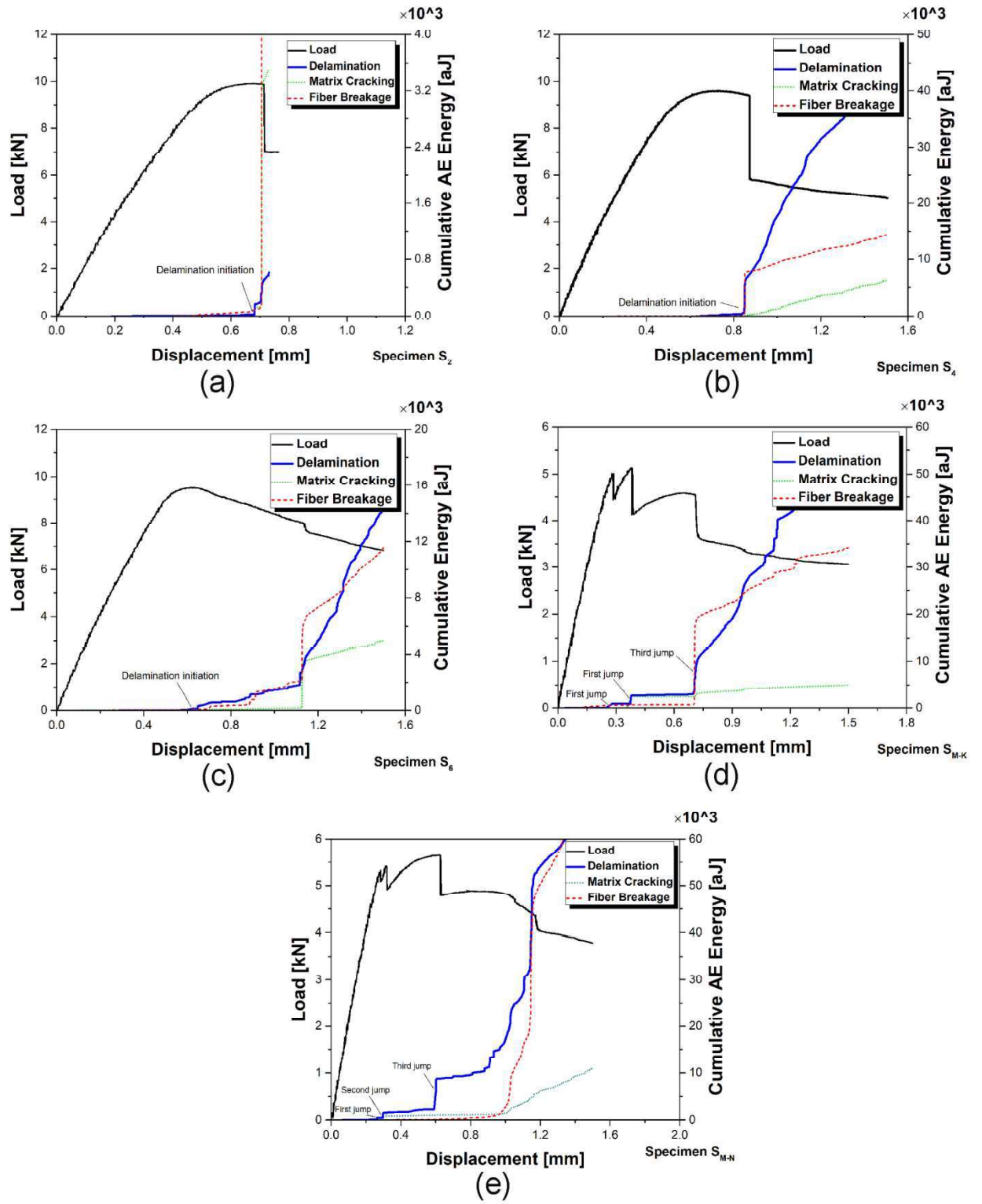


Fig. 15. The cumulative AE energy of different damage mechanisms for specimens a) S_2 , b) S_4 , c) S_6 , d) S_{M-K} , and e) S_{M-N} .

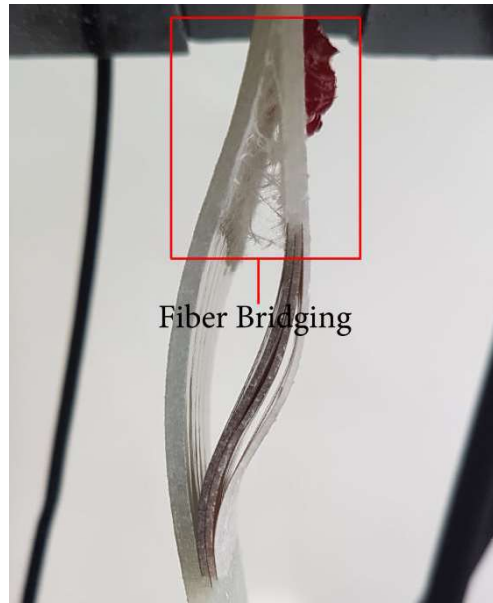


Fig. 16. The fiber bridging phenomenon in specimen S_{M-K} .

Table 3 reports the corresponding vertical displacement to the delaminations growth in the specimens identified by different methods. As can be seen, the AE-based methods (i.e. AE energy, AE cumulative count, and sentry function) recognize the delamination growth earlier than the other conventional methods (i.e. visual detection method and the load drop method). The vertical displacements corresponding to delamination growth which were detected by AE are about 17% lower than the displacements predicted by the conventional methods on average of all specimens. The visual detection method offers the upper bound results due to difficulties of visual detection of delamination growth. The load drop method does not offer a good result for specimen S_6 as its load decreases gradually without significant instantaneous drop. In addition, the variance of the AE-based results is about 68% lower than the variance of the conventional methods results (see Fig. 17). Thus, AE can be used in health monitoring of the laminated composite structures subjected to compression loading.

Table 3. The corresponding vertical displacement to the delamination growth in the specimens identified by different methods.

Specimen	Delamination number	Visual detection	Load drop	AE-based methods			
				AE energy	Cumulative AE count	Sentry function	Cumulative energy of delamination signals
S _P	-	-	-	-	-	-	-
S ₂	2 nd	0.81	0.72	0.71	0.70	0.70	0.68
S ₄	4 th	0.98	0.88	0.86	0.85	0.65	0.82
S ₆	6 th	0.98	1.14	0.60	0.60	0.59	0.60
S _{M-K}	2 nd	0.36	0.30	0.28	0.26	0.26	0.24
	4 th	0.46	0.39	0.38	0.37	0.38	0.36
	6 th	0.80	0.72	0.71	0.70	0.71	0.70
S _{M-N}	2 nd	0.38	0.29	0.26	0.26	0.30	0.26
	4 th	0.43	0.32	0.30	0.30	0.32	0.30
	6 th	0.74	0.63	0.60	0.60	0.60	0.59

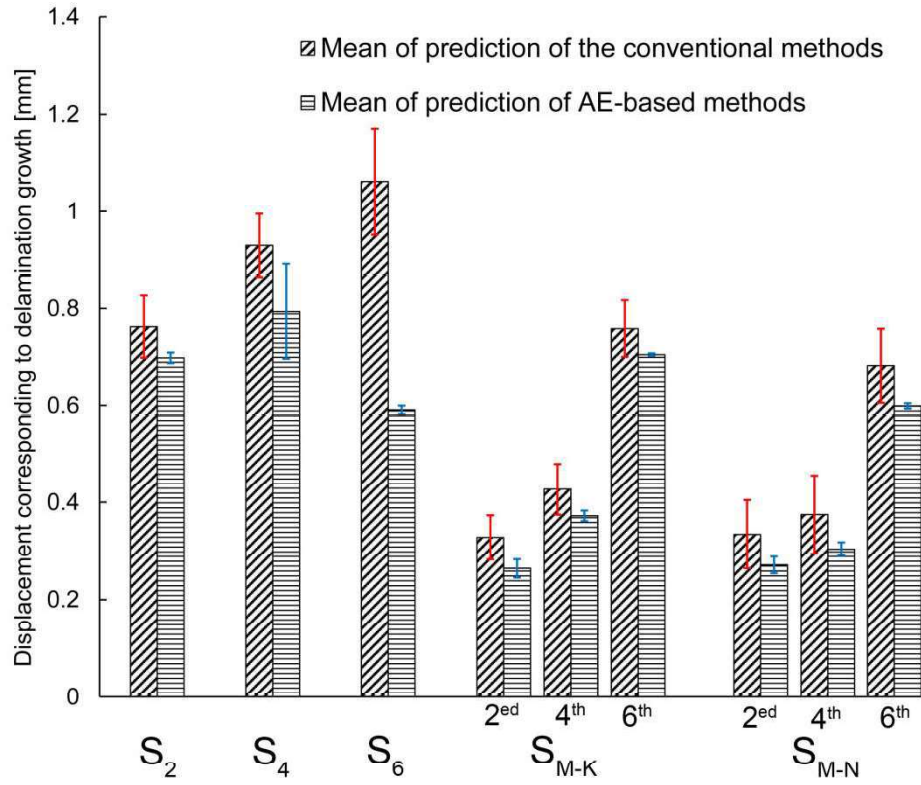


Fig. 17. The Mean value and standard deviation of identified displacement corresponding to delamination growth by the conventional methods (visual detection and load drop) and AE-based methods (AE energy, cumulative AE count, sentry function, and cumulative energy of delamination signals).

5. Conclusions

In this study, the effects of location, thickness and number of multiple delaminations on buckling and post-buckling behavior of glass/epoxy composites were investigated using mechanical and AE analysis. Different types of laminates, with and without pre-delaminations and with different numbers and locations of the pre-delaminations and different thicknesses of Teflon film as the artificial delamination were studied. Mechanical results showed that when the artificial delamination is closer to the specimen's surface; the load decreases faster after the maximum load, and the final displacement before final failure reduces. The critical and maximum loads are also reduced by increasing the thickness of the Teflon film, i.e. thickness of the artificial

delamination. Due to the importance of delamination growth in the post-buckling analyses of the laminate, different approaches based on AE were applied to accurately detect the point of delamination growth. In addition, GMM was utilized to cluster the AE signals to identify the different damage types occurred during the buckling tests and to determine the evolution of each damage mechanism. The vertical displacements corresponding to delamination growth which were detected by AE were about 17% lower than the displacement predicted by the conventional methods (i.e. visual detection and load drop methods) and also the standard deviation of the AE predictions was about 68% lower than from the standard deviation of the predictions of the other conventional methods. Finally, it is concluded that AE is a robust technique for detection of delamination growth and monitoring the damage evolution in buckling of laminated composites

References

- [1] Sridharan S. Delamination behavior of composites. New York; CRC Press: 2008.
- [2] Panda HS, Sahu SK, Parhi PK. Effects of moisture on the frequencies of vibration of woven fibre composite doubly curved panels with strip delaminations. Thin Walled Struct 2014; 78: 79-86.
- [3] Saeedifar S, Fotouhi M, Ahmadi Najafabadi M, Hossein Hosseini Toudeshky H, Minak G. Prediction of quasi-static delamination onset and growth in laminated composites by acoustic emission. Composites Part B 2016; 85: 113-22.
- [4] Benmedakhene S, Kenane M, Benzeggagh ML. Initiation and growth of delamination in glass/epoxy composites subjected to static and dynamic loading by acoustic emission monitoring. Compos Sci Technol 1991; 59: 201–8.
- [5] Loutas T, Eleftheroglou N, Zarouchas D. A data-driven probabilistic framework towards the in-situ prognostics of fatigue life of composites based on acoustic emission data. Compos Struct 2017; 161: 522–9.

- [6] Pawar PM. On the behavior of thin walled composite beams with stochastic properties under matrix cracking damage. *Thin Walled Struct* 2011; 49(9): 1123-31.
- [7] Liu PF, Gu ZP, Peng XQ, Zheng JY. Finite element analysis of the influence of cohesive law parameters on the multiple delamination behaviors of composites under compression. *Compos Struct* 2015; 131: 975–86.
- [8] Sun G, Zhou Z. Application of laser ultrasonic technique for non-contact detection of drilling-induced delamination in aeronautical composite components. *Optik* 2014;125:3608–11
- [9] Senthil K, Arockiarajan A, Palaninathan R, Santhosh B, Usha KM. Investigations on adhesively bonded curved CFRP panels with closed debonds subjected to compressive load. *Thin Walled Struct* 2014; 85: 367-76.
- [10] Liu P, Groves RM, Benedictus R. 3D monitoring of delamination growth in a wind turbine blade composite using optical coherence tomography. *NDT&E Int* 2014;64:52–8.
- [11] Amenabar I, Mendikute A, López-Arraiza A, Lizaranzu M, Aurrekoetxea J. Comparison and analysis of non-destructive testing techniques suitable for delamination inspection in wind turbine blades. *Composites Part B* 2011; 42(5): 1298-305.
- [12] Mohammadi R, Saeedifar M, Hosseini Toudeshky H, Ahmadi Najafabadi M, Fotouhi M. Prediction of delamination growth in carbon/epoxy composites using a novel acoustic emission-based approach. *J Reinf Plast Compos* 2015; 34(11): 868-78.
- [13] Amaral L, Zarouchas D, Alderliesten R, Benedictus R,. Energy dissipation in mode II fatigue crack growth. *Eng Fract Mech* 2017; 173: 41-54.
- [14] Teter A, Debski H, Samborski S. On buckling collapse and failure analysis of thin-walled composite lipped-channel columns subjected to uniaxial compression. *Thin Walled Struct* 2014; 85: 324-31.
- [15] Yousefi J, Mohamadi R, saeedifar M, Ahmadi M, Toudeshky H. Delamination characterization in composite laminates using acoustic emission features, micro visualization and finite element modeling. *J Compos Mater* 2015; DOI: 10.1177/0021998315615691.
- [16] Parlapalli MR, Soh KC, Shu DW, Ma G. Experimental investigation of delamination buckling of stitched composite laminates. *Composites Part A* 2007; 38(9): 2024–33.

- [17] Ovesy HR, Asghari Mooneghi M, Kharazi M. Post-buckling analysis of delaminated composite laminates with multiple through-the-width delaminations using a novel layerwise theory. *Thin Walled Struct* 2015; 94: 98-106.
- [18] Horban B, Palazotto A. Experimental buckling of cylindrical composite panels with eccentrically located circular delaminations. *J Space Rock* 1987; 24(4): 349-52.
- [19] Craven R, Iannucci L, Olsson R. Delamination buckling: A finite element study with realistic delamination shapes, multiple delaminations and fibre fracture cracks. *Composites Part A* 2010; 41: 684–92.
- [20] Hosseini Toudeshky H, Hosseini S, Mohammadi B. Delamination buckling growth in laminated composites using layerwise-interface element. *Compos Struct* 201; 92:1846–56.
- [21] Gu H, Chattopadhyay A. An experimental investigation of delamination buckling and post-buckling of composite laminates. *Compos Sci Technol* 1999; 59(6): 903–10.
- [22] Saeedifar M, Fotouhi M, Ahmadi Najafabadi M, Hosseini Toudeshky H. Prediction of delamination growth in laminated composites using acoustic emission and cohesive zone modeling techniques. *Compos Struct* 2015; 94 (5): 1483–94.
- [23] Romhany G, Szebényi G. Interlaminar fatigue crack growth behavior of MWCNT/carbon fiber reinforced hybrid composites monitored via newly developed acoustic emission method. *Express Polym Lett* 2012;6(7):572–80.
- [24] Mechraoui SE, Laksimi A, Benmedakhene S. Reliability of damage mechanism localisation by acoustic emission on glass/epoxy composite material plate. *Compos Struct* 2012;94(5):1483–94.
- [25] Mohammadi R, Ahmadi Najafabadi M, Saeedifar M, Yousefi J, Minak G. Correlation of acoustic emission with finite element predicted damages in open-hole tensile laminated composites. *Composites Part B* 2017; 108: 427-35.
- [26] Paget CA. Delamination location and size by modified acoustic emission on cross-ply CFRP laminates during compression-compression fatigue loading. In: *ICCM17 proceedings*, UK; 2009.

- [27] Saeedifar M, Fotouhi M, Ahmadi Najafabadi M, Hosseini Toudeshky H. Interlaminar fracture toughness evaluation in glass/epoxy composites using acoustic emission and finite element methods. *J Mater Eng Perform* 2015; 24(1): 373-84.
- [28] McCrory JP, Al-Jumaili SK, Crivelli D, Pearson MR, Eaton MJ, et al. Damage classification in carbon fibre composites using acoustic emission: a comparison of three techniques. *Composites Part B* 2015; 68:424–30.
- [29] Debski H, Teter A, Kubiak T, Samborski S. Local buckling, post-buckling and collapse of thin-walled channel section composite columns subjected to quasi-static compression. *Compos Struct* 2016; 136: 593–601.
- [30] Zhou W, Lv Z, Li Z, Song X. Acoustic emission response and micro-deformation behavior for compressive buckling failure of multi-delaminated composites. *J Strain Analysis* 2016; 51(6):1-11.
- [31] Bishop CM. *Pattern Recognition and Machine Learning*. Springer Science+Business Media, Singapore, 2006; 430-55.
- [32] Aslan Z, Daricik F. Effects of multiple delaminations on the compressive, tensile, flexural, and buckling behaviour of E-glass/epoxy composites. *Composites Part B* 2016; 100: 186-96.
- [33] Xue JH, Luo QZ, Han F, Liu RH. Two-dimensional analyses of delamination buckling of symmetrically cross-ply rectangular laminates. *Appl Math Mech* 2013; 34(5): 597–612.
- [34] Refahi Oskoue A, Zucchelli A, Ahmadi M, Minak G. An integrated approach based on acoustic emission and mechanical information to evaluate the delamination fracture toughness at mode I in composite laminate. *Mater Des* 2011; 32(3): 1444-55.
- [35] Fotouhi M, Heidary H, Ahmadi M, Pashmforoush F. Characterization of composite materials damage under quasi-static three-point bending test using wavelet and fuzzy C-means clustering. *J Compos Mater* 2012; 46(15): 1795-808.
- [36] Pashmforoush F, Khamedi R, Fotouhi M, Hajikhani M, Ahmadi M. Damage classification of sandwich composites using acoustic emission technique and k-means genetic algorithm. *J Nondestr Eval* 2014; 33 (4): 481-92.
- [37] Vesanto J, Alhoniemi E. Clustering of the Self-Organizing Map. *IEEE Trans Neural Networks* 2000; 11(3): 586-600.

- [38] Fotouhi M, Saeedifar M, Sadeghi S, Ahmadi Najafabadi M, Minak G. Investigation of the damage mechanisms for mode I delamination growth in foam core sandwich composites using acoustic emission. Struct Health Monit 2015; 14(3): 1-16.

List of Figure captions

Fig. 1. The schematic of the specimens.

Fig. 2. a) The schematic and b) the real test setup.

Fig. 3. The compression load vs. vertical displacement curve of specimens S_P .

Fig. 4. The compression load vs. vertical displacement curve of specimens a) S_6 , b) S_4 , and c) S_2 .

Fig. 5. The compression load vs. vertical displacement curve of specimens a) S_{M-K} and b) S_{M-N} .

Fig. 6. The growth of a) first, b) second, and c) third delamination in specimen S_{M-K} .

Fig. 7. Load vs. normalized lateral deflection (lateral deflection divided to the specimen's thickness) curve of the specimens a) S_P , S_2 , S_4 , and S_6 , and b) S_{M-K} , and S_{M-N} . (Base-laminate which is denoted by "Base" is the thicker part of the specimen at the side of delamination and sub-laminate which is denoted by "Sub" is the slender part of the specimen at the other side of delamination).

Fig. 8. The ratio of the critical and maximum loads of the specimens to the critical and maximum loads of specimen S_P with the standard deviation.

Fig. 9. a) The AE energy and b) the cumulative AE count curves of specimen S_4 .

Fig. 10. a) The AE energy and b) the cumulative AE count of specimen S_{M-K} .

Fig. 11. The sentry function curves of specimens a) S_{M-K} and b) S_4 .

Fig. 12. The optimum clusters number for AE signals of the specimens.

Fig. 13. The clustering of AE signals by GMM for specimens a) S_2 , b) S_4 , c) S_6 , d) S_{M-K} , and e) S_{M-N} .

Fig. 14. The peak frequency range of the AE signals of a) delamination, b) matrix cracking, and c) fiber breakage [37].

Fig. 15. The cumulative AE energy of different damage mechanisms for specimens a) S_2 , b) S_4 , c) S_6 , d) S_{M-K} , and e) S_{M-N} .

Fig. 16. The fiber bridging phenomenon in specimen S_{M-K} .

Fig. 17. The Mean value and standard deviation of identified displacement corresponding to delamination growth by the conventional methods (visual detection and load drop) and AE-based methods (AE energy, cumulative AE count, sentry function, and cumulative energy of delamination signals).

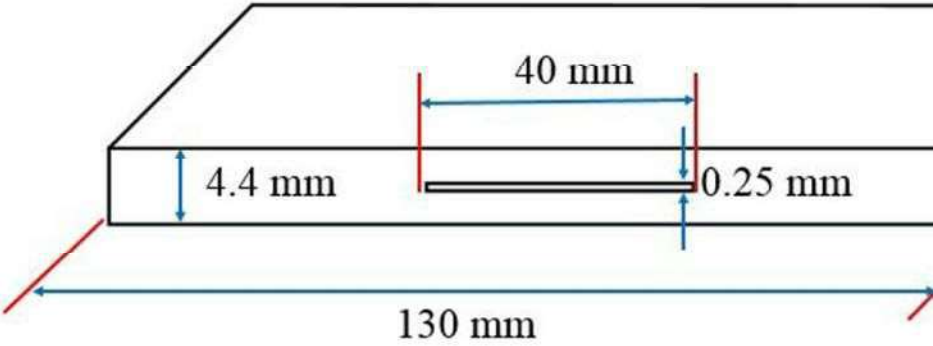
List of Table captions

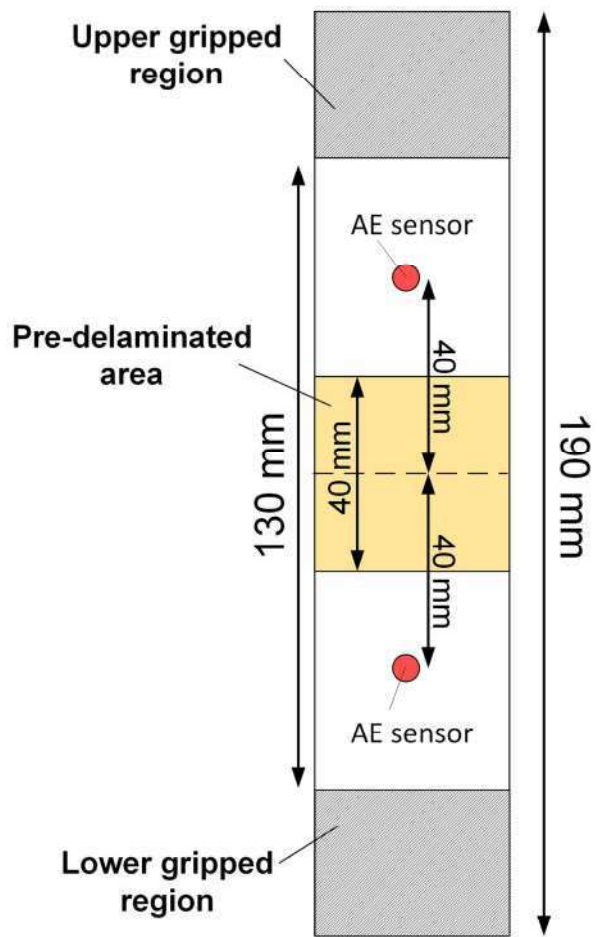
Table 1. The specifications of the specimens.

Table 2. The effects of the number and the location of delamination on critical buckling load and maximum load of the specimens.

Table 3. The corresponding vertical displacement to the delamination growth in the specimens identified by different methods.

0°	1
90°	2
0°	3
90°	4
0°	5
90°	6
0°	7
90°	8
0°	9
90°	10
0°	11
90°	

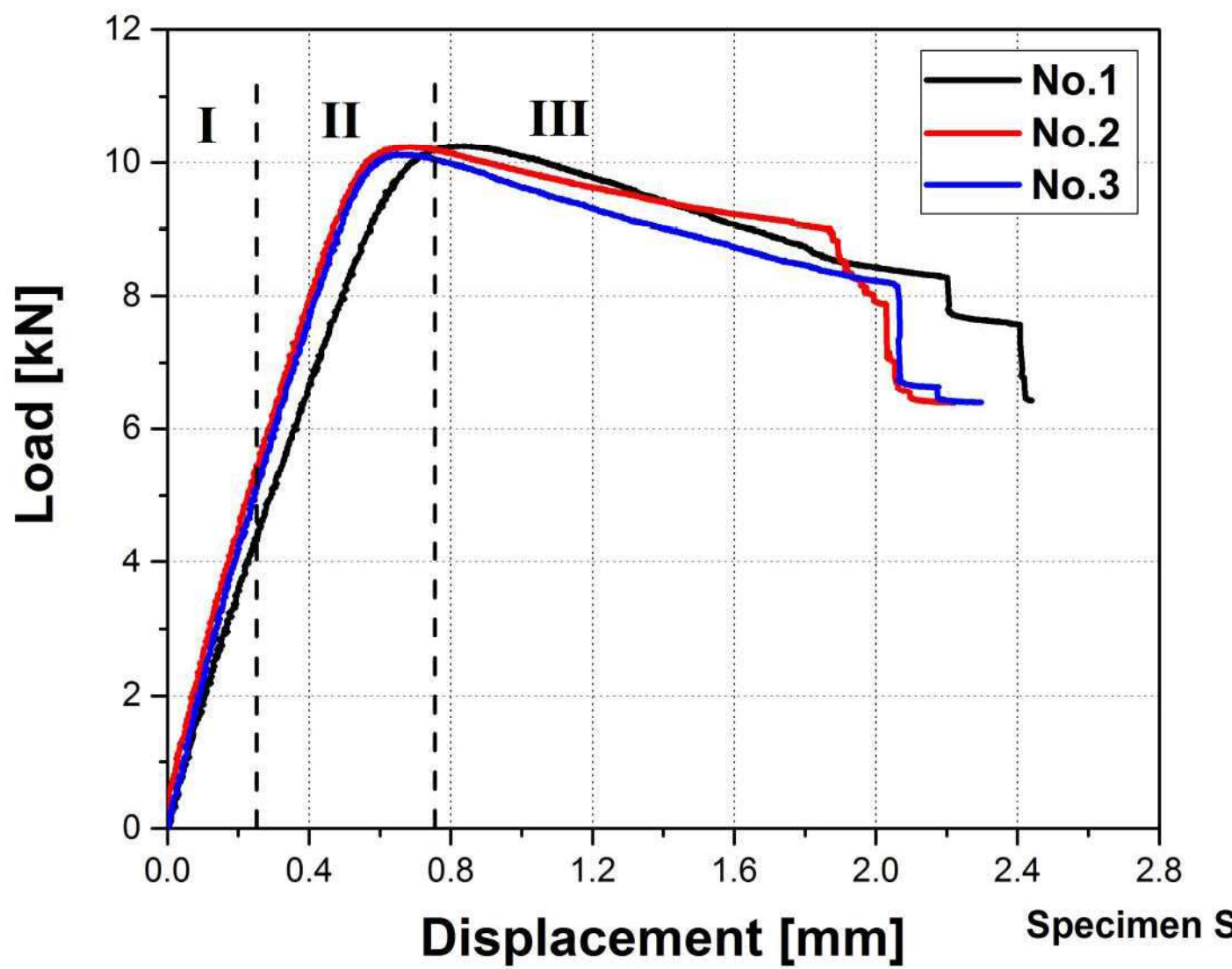


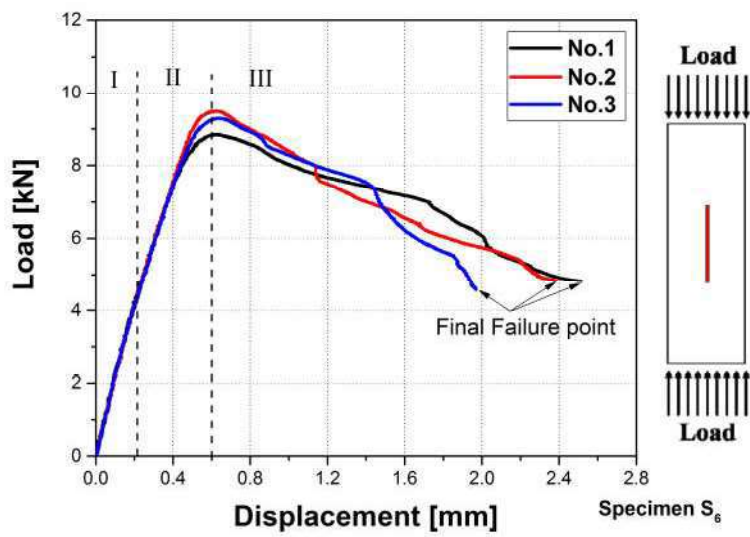


(a)

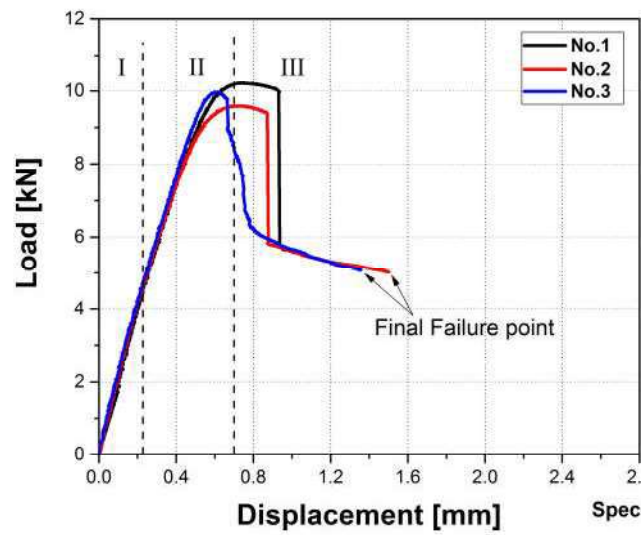


(b)

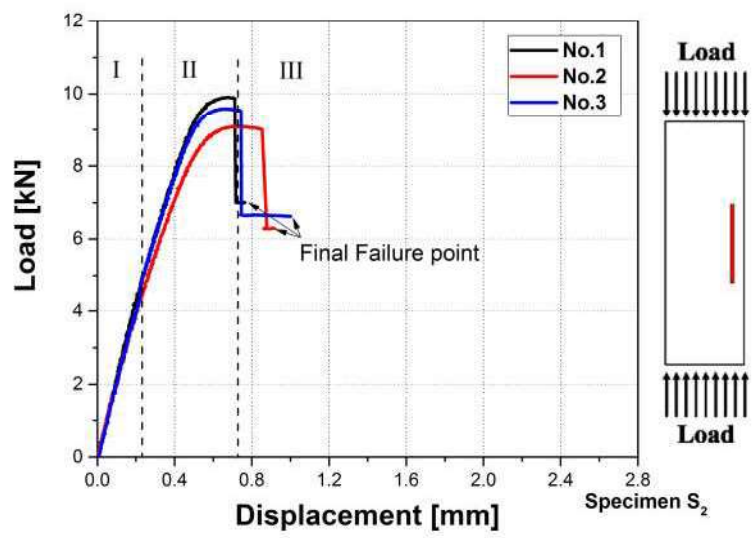




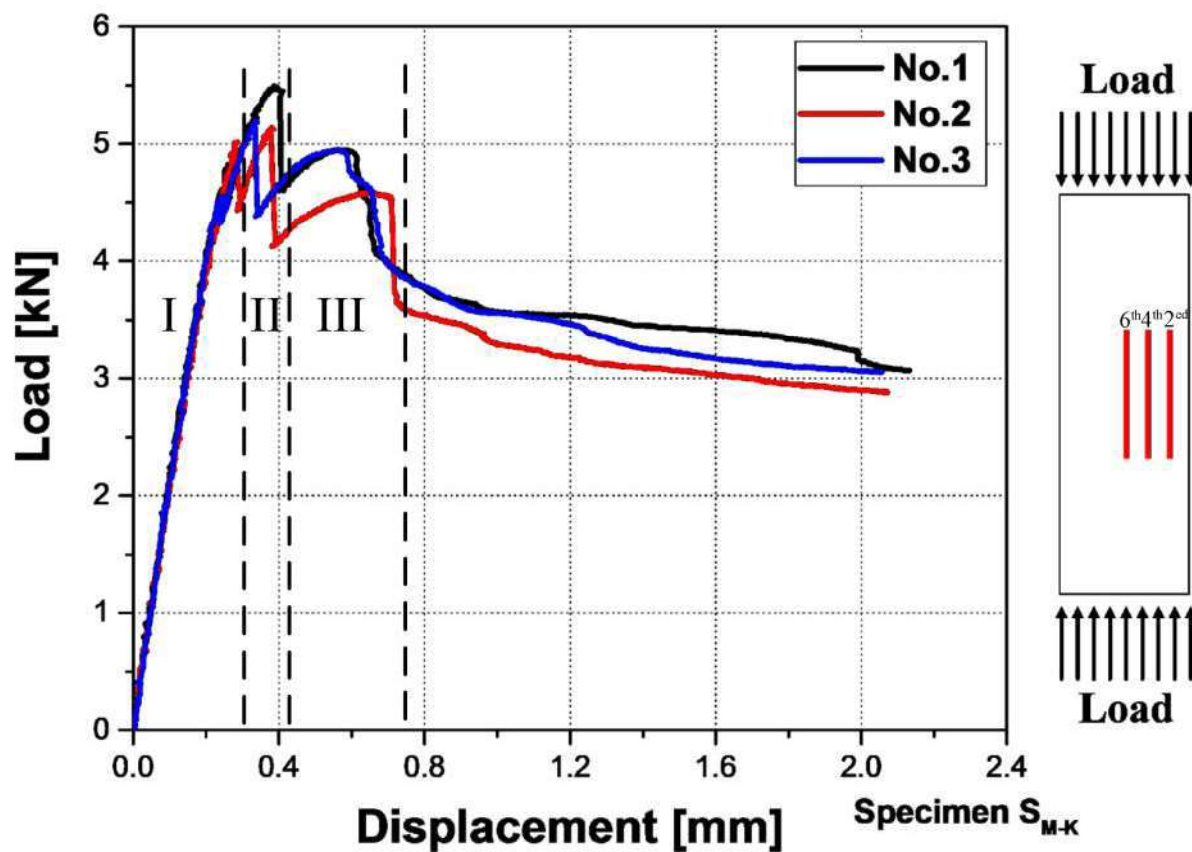
(a)



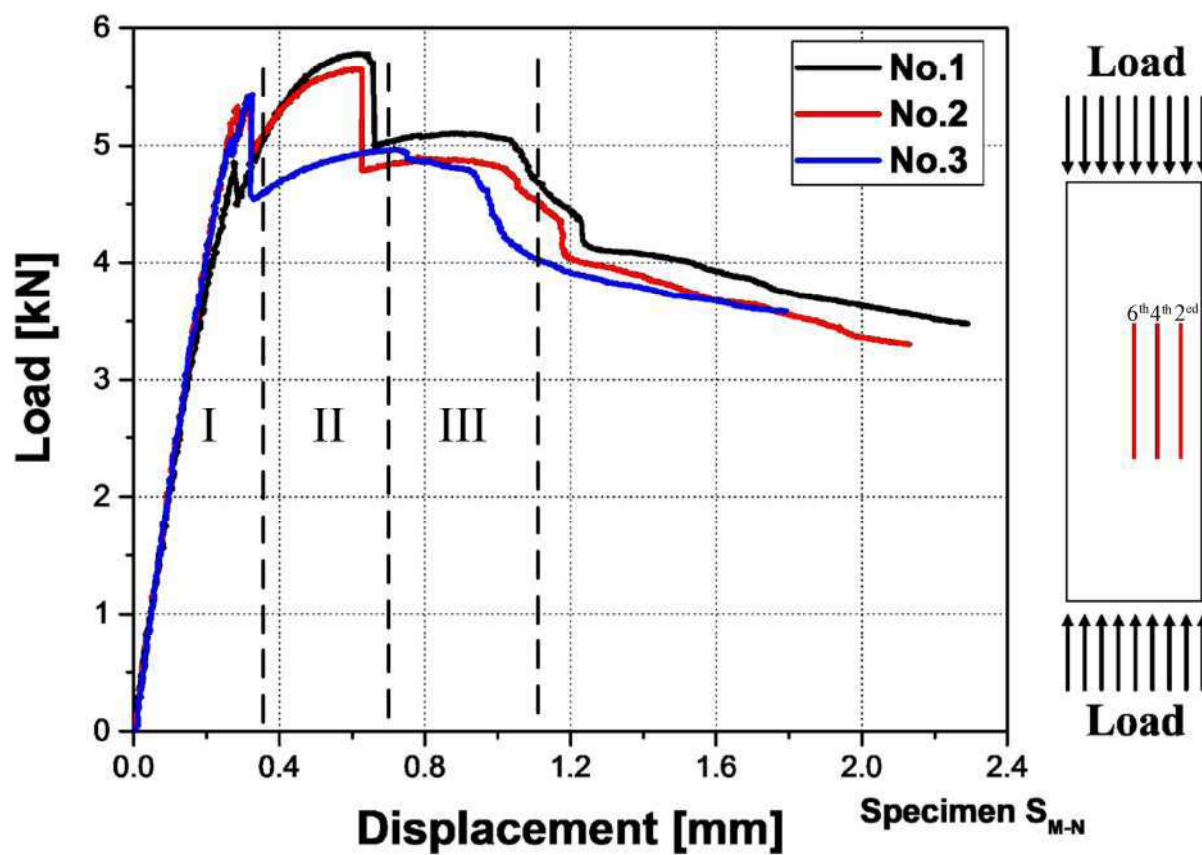
(b)



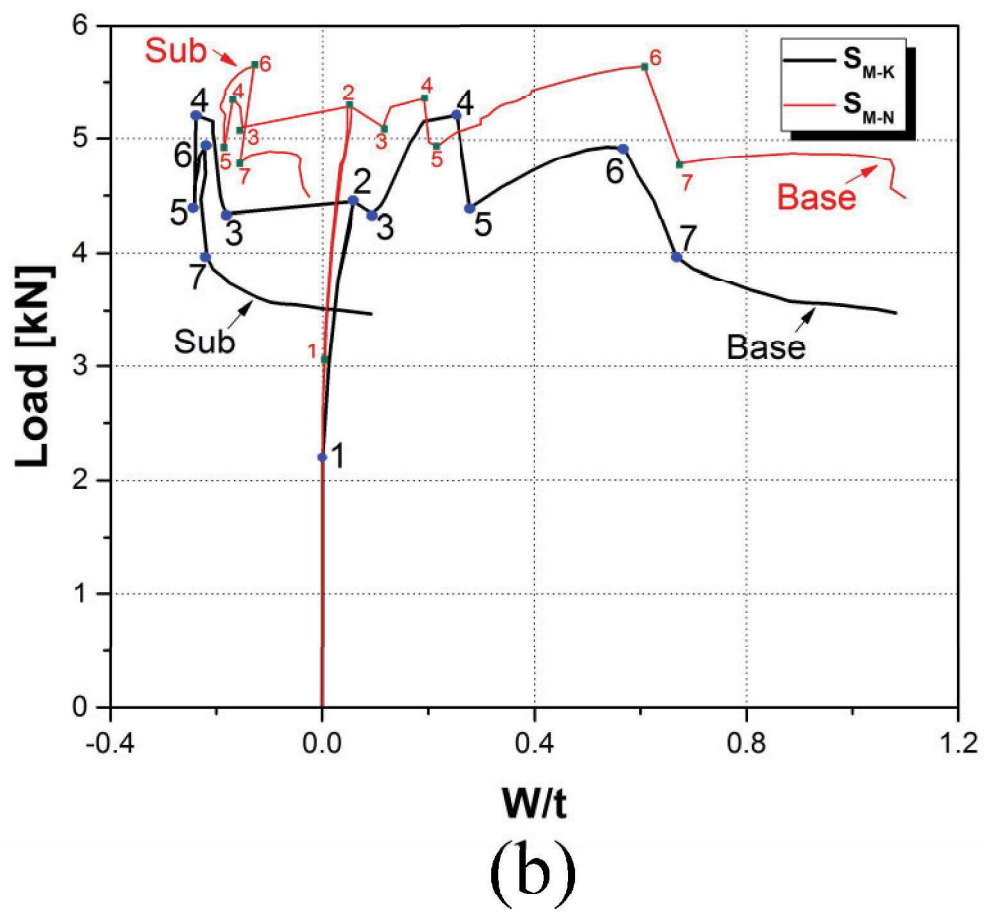
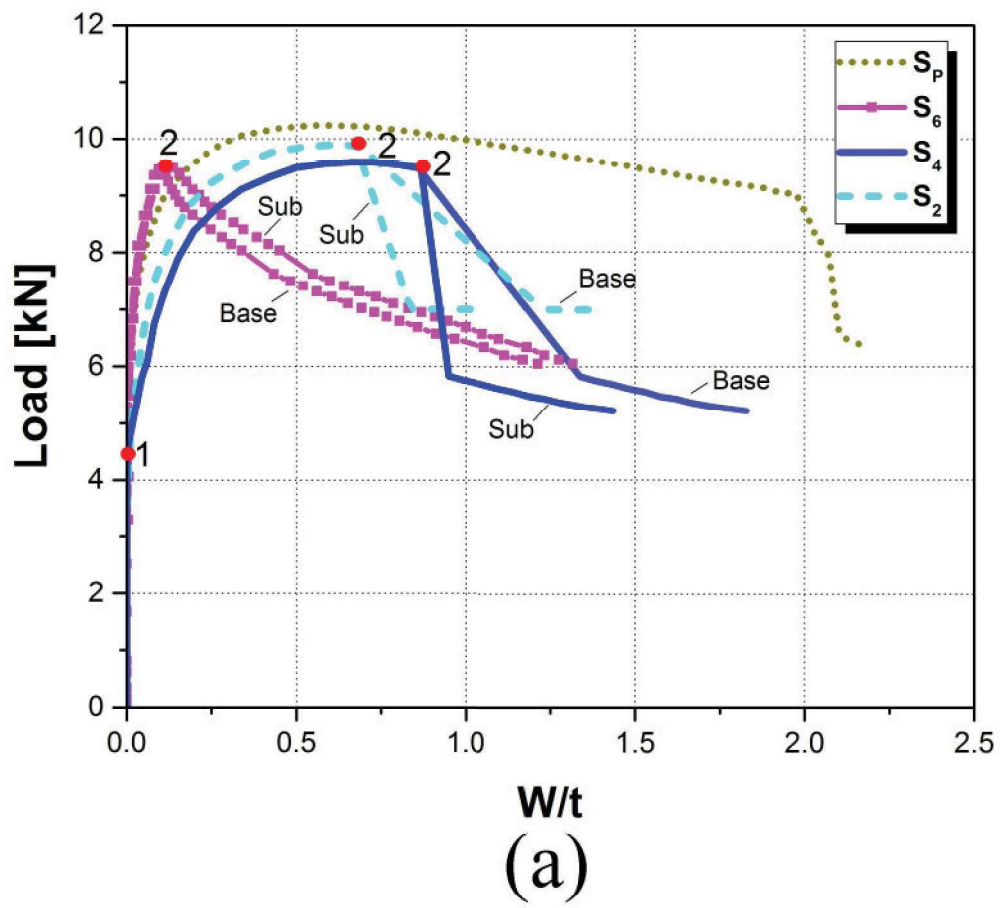
(c)

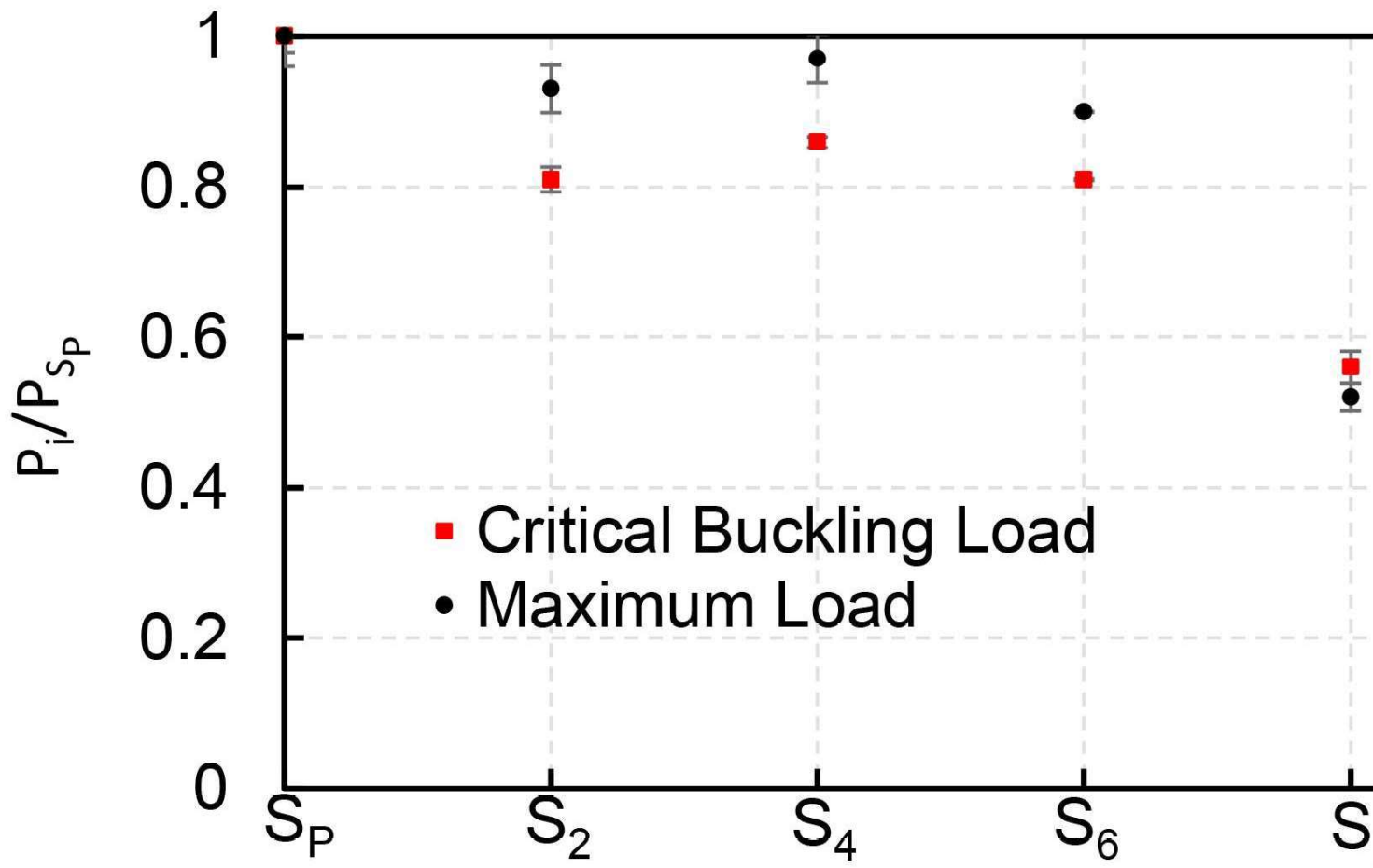


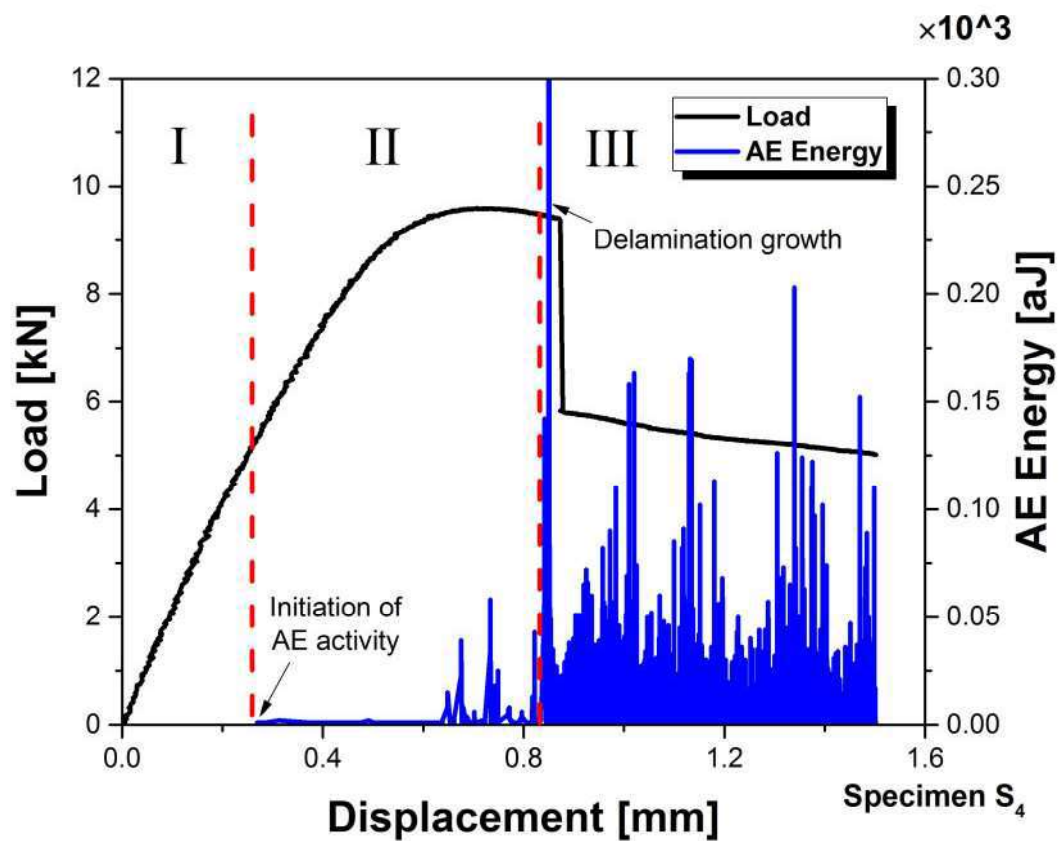
(a)



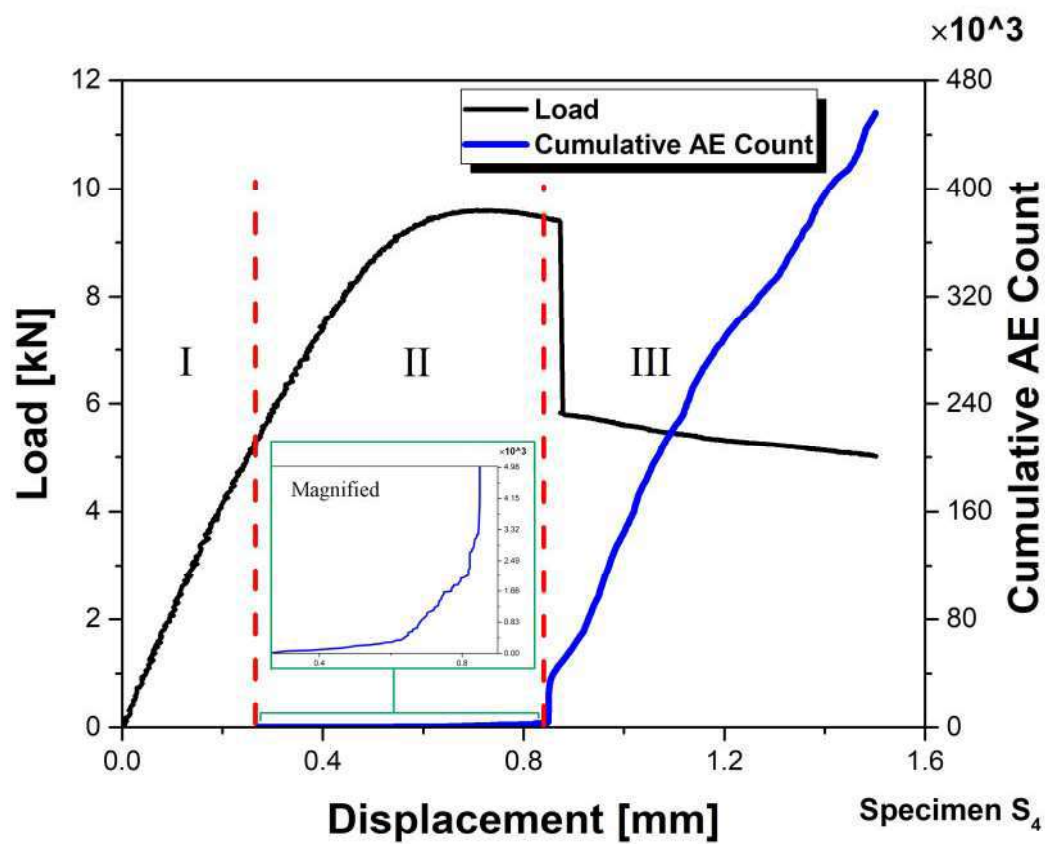
(b)



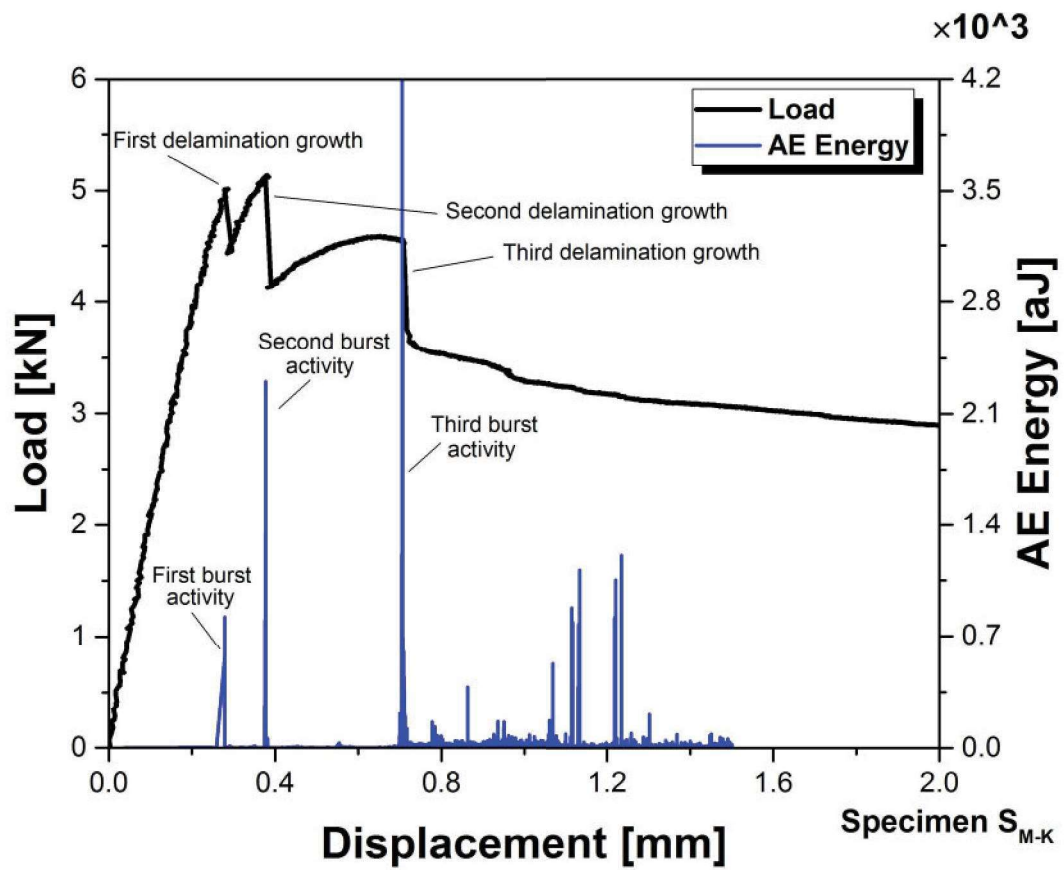




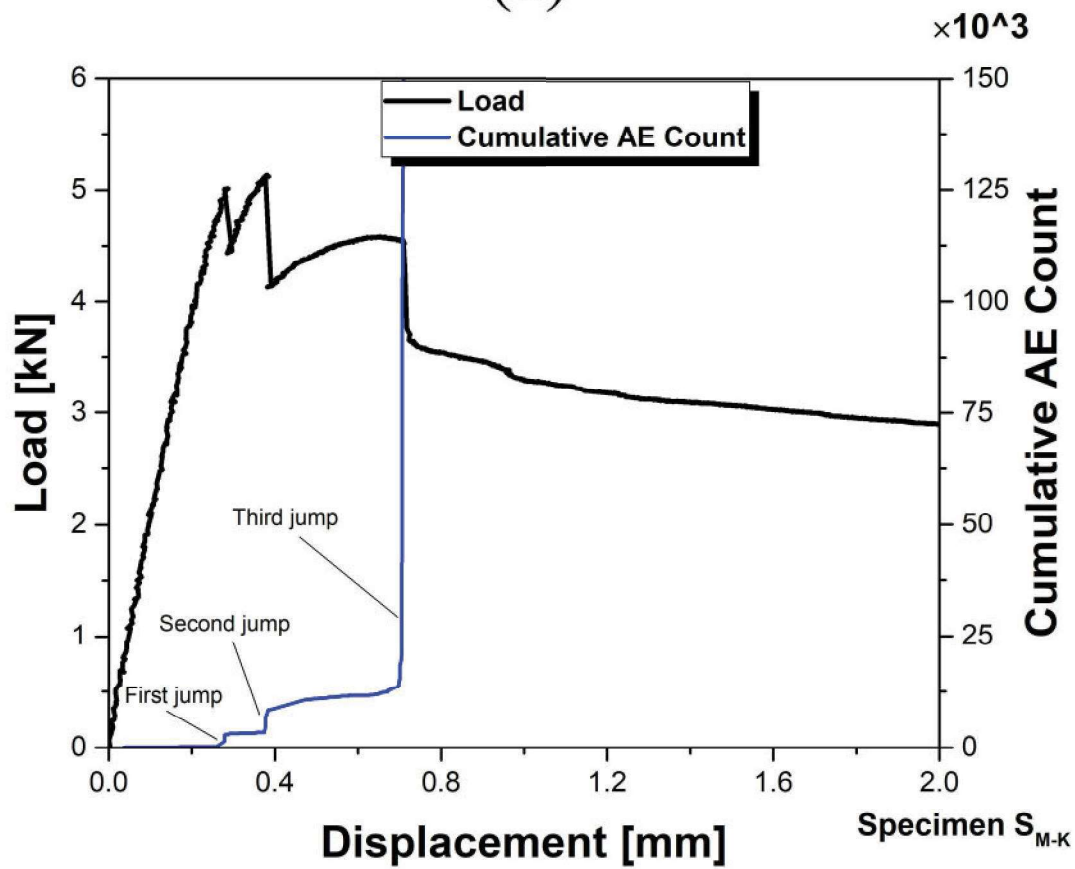
(a)



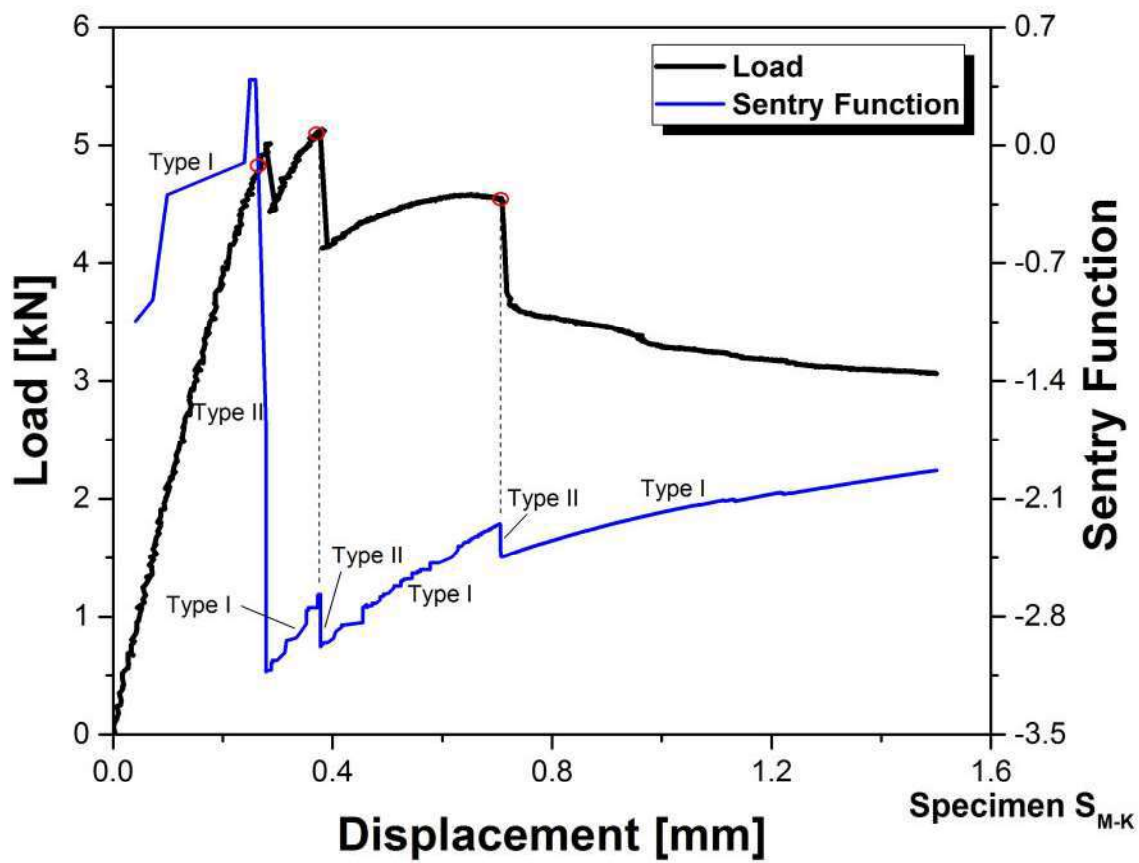
(b)



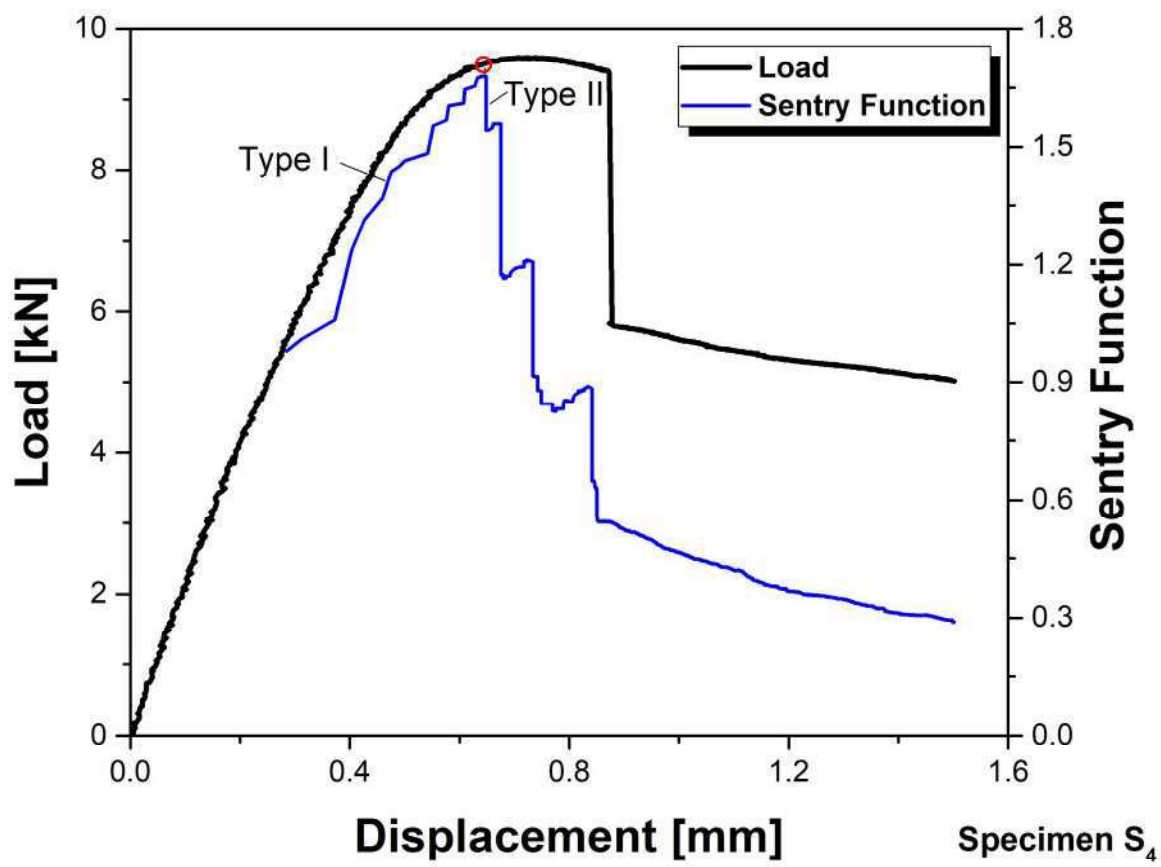
(a)



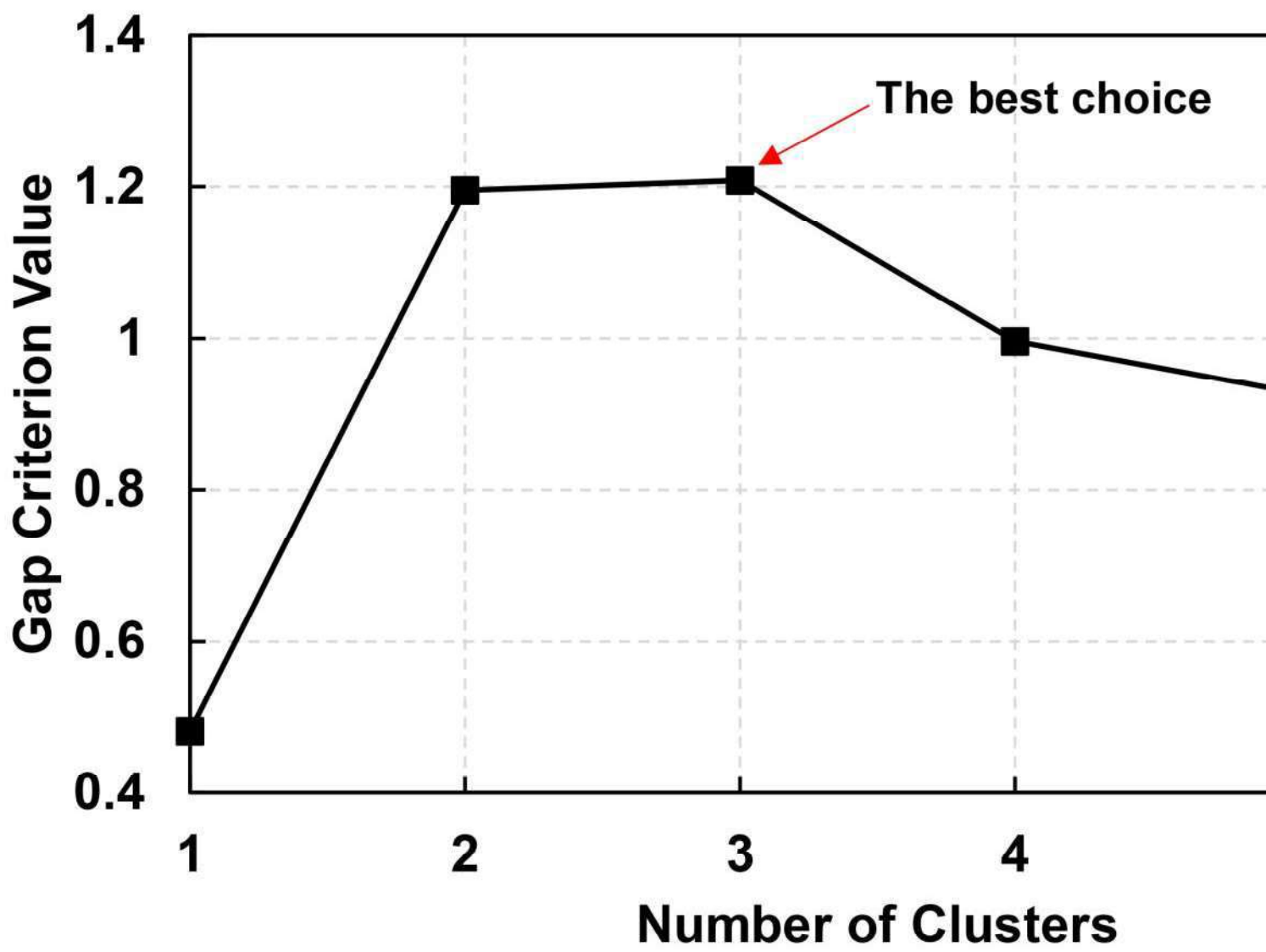
(b)

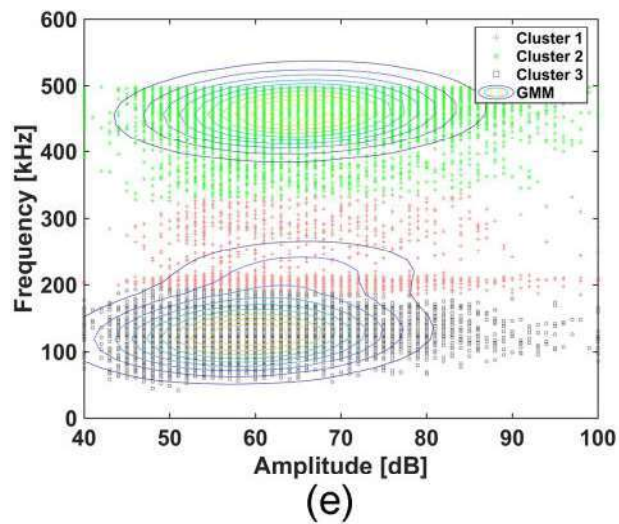
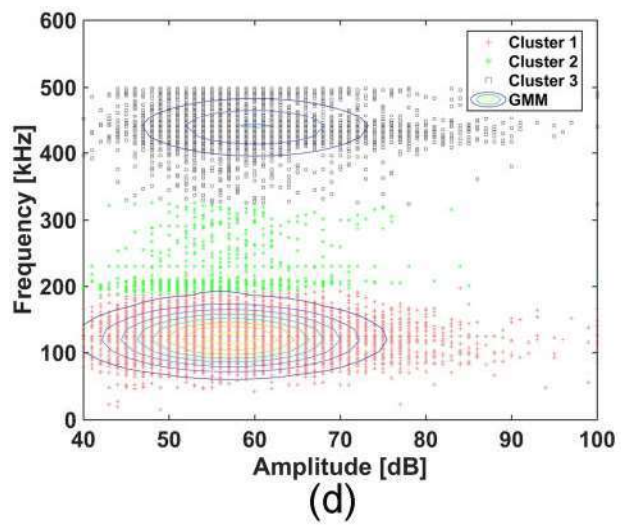
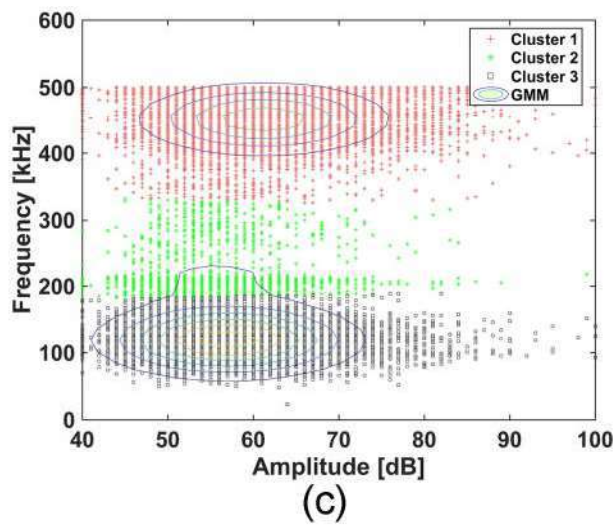
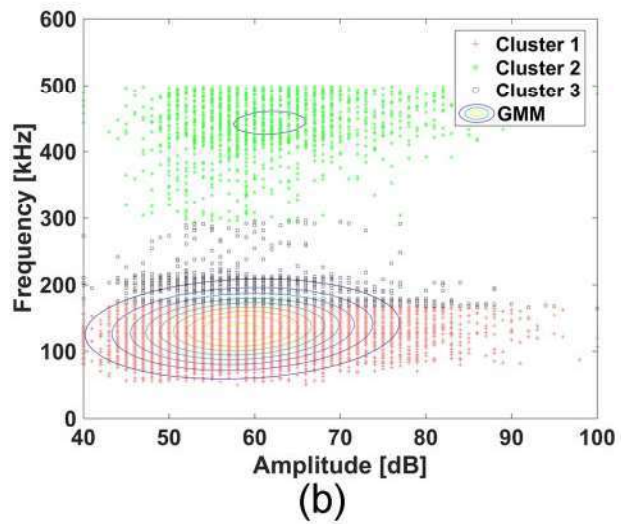
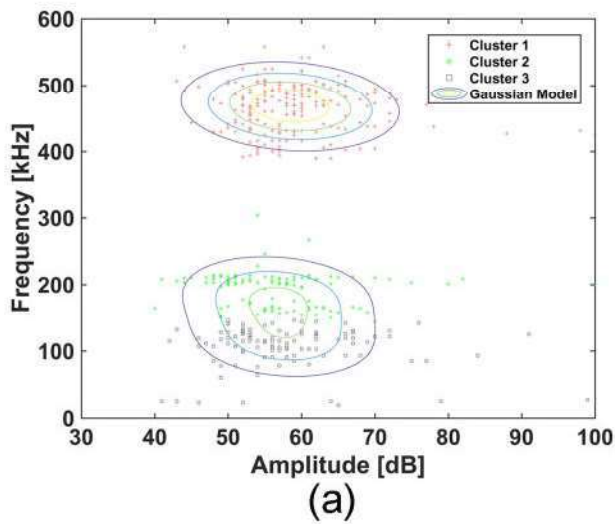


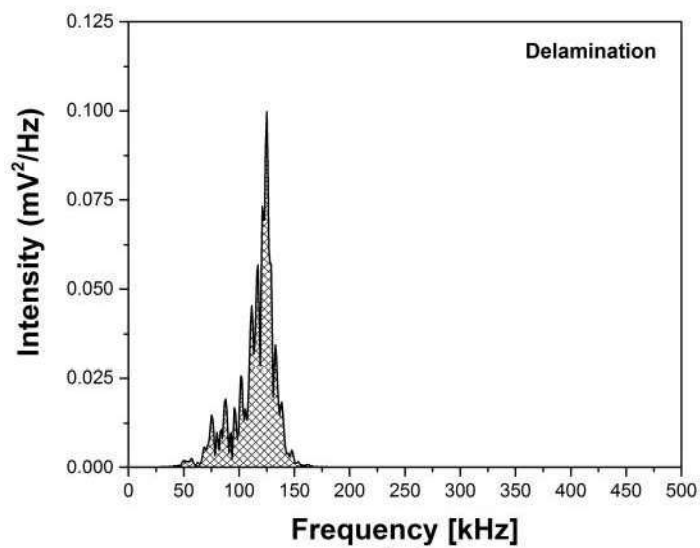
(a)



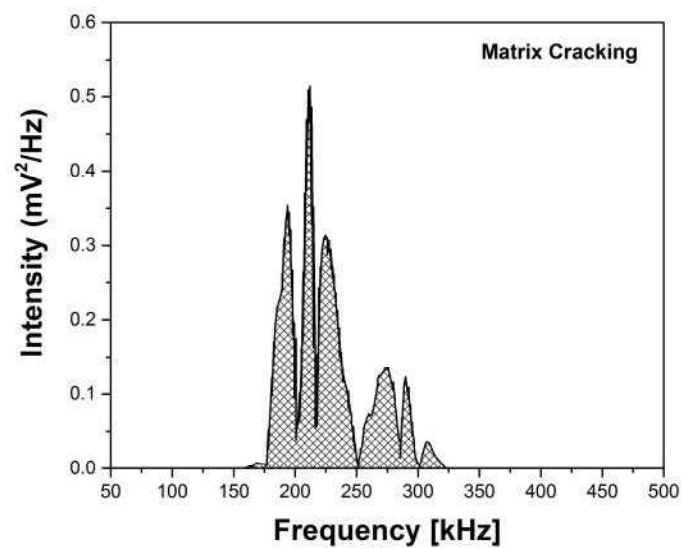
(b)



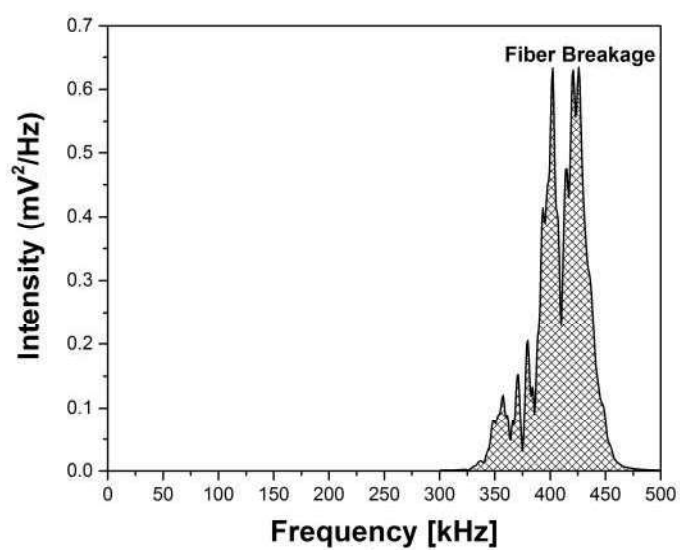




(a)



(b)



(c)

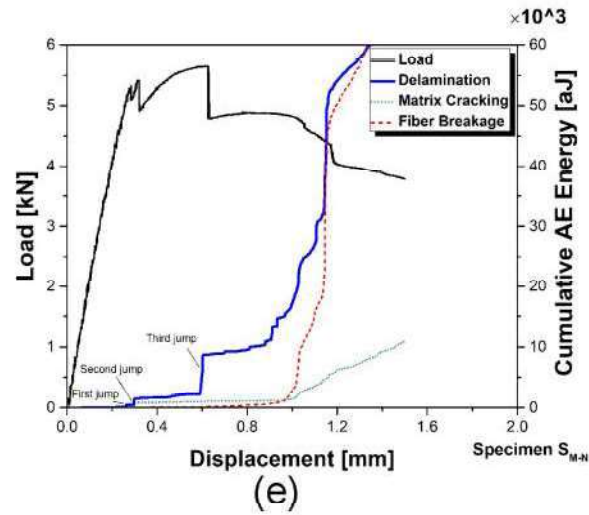
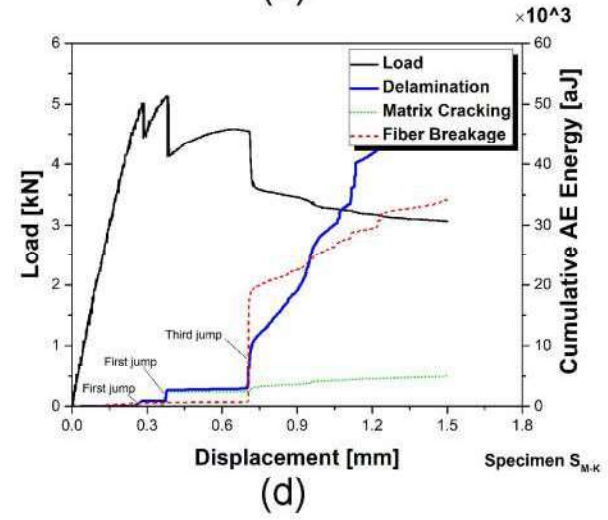
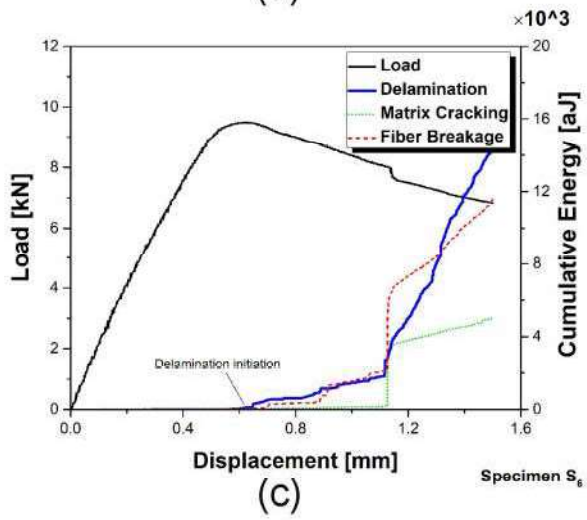
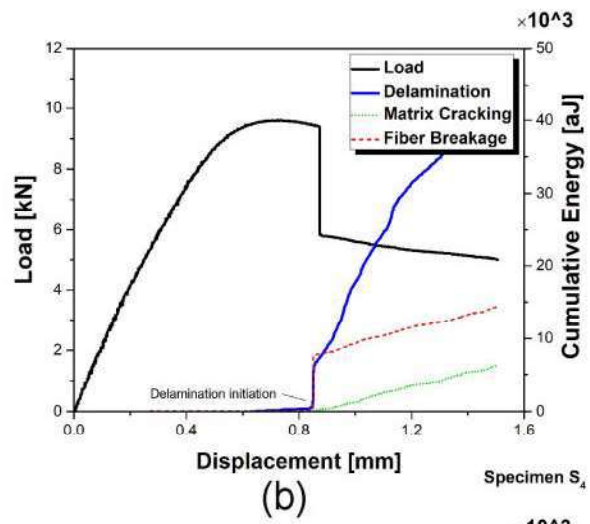
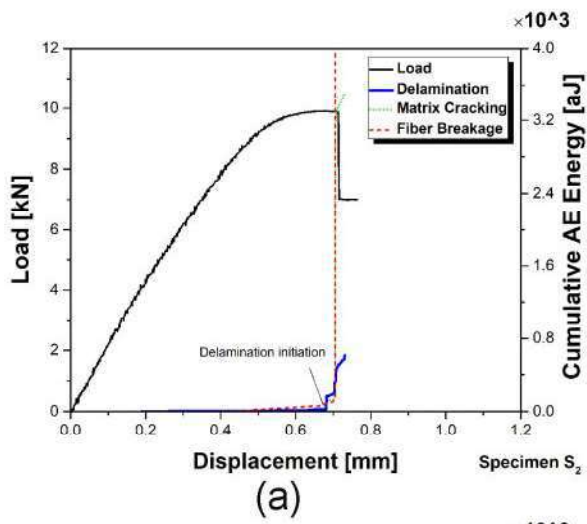


Table 1. The specifications of the specimens.

Specimens	Delamination location	The thickness of Teflon film that serves as the artificial delamination (μm)	Lay-ups
S _p	Without pre-delamination	-	$[0^\circ / 90^\circ]_6$
S ₂	2 nd interface	250	$[0^\circ / 90^\circ]_6$
S ₄	4 th interface	250	$[0^\circ / 90^\circ]_6$
S ₆	6 th interface	250	$[0^\circ / 90^\circ]_6$
S _{M-K}	2 nd , 4 th , and 6 th interfaces	250	$[0^\circ / 90^\circ]_6$
S _{M-N}	2 nd , 4 th , and 6 th interfaces	150	$[0^\circ / 90^\circ]_6$

Table 2. The effects of the number and the location of delamination on critical buckling load and maximum load of the specimens.

Specimen	Sample No.	P_{cr}	P_{Max}	Mean of P_{cr}	Mean of P_{Max}	$\frac{P_{cr}}{P_{Max}}$	$\frac{P_{cr-i}}{P_{cr-Sp}}$	$\frac{P_{Max-i}}{P_{Max-Sp}}$
S_p	Sample 1	5.15	10.24	5.23	10.21	0.51	1	1
	Sample 2	5.21	10.26					
	Sample 3	5.32	10.13					
S_2	Sample 1	4.30	9.91	4.24	9.53	0.44	0.81	0.93
	Sample 2	4.11	9.09					
	Sample 3	4.31	9.60					
S_4	Sample 1	4.56	9.59	4.52	9.93	0.45	0.86	0.97
	Sample 2	4.58	9.97					
	Sample 3	4.42	10.22					
S_6	Sample 1	4.21	9.49	4.23	9.21	0.46	0.81	0.90
	Sample 2	4.21	9.29					
	Sample 3	4.27	8.85					
S_{M-K}	Sample 1	2.94	5.13	2.93	5.27	0.56	0.56	0.52
	Sample 2	2.93	5.49					
	Sample 3	2.93	5.20					
S_{M-N}	Sample 1	3.00	5.65	3.12	5.62	0.56	0.60	0.55
	Sample 2	3.22	5.78					
	Sample 3	3.14	5.43					

Table 3. The corresponding vertical displacement to the delamination growth in the specimens identified by different methods.

Specimen	Delamination number	Visual detection	Load drop	AE-based methods			
				AE energy	Cumulative AE count	Sentry function	Cumulative energy of delamination signals
S _p	-	-	-	-	-	-	-
S ₂	2 nd	0.81	0.72	0.71	0.70	0.70	0.68
S ₄	4 th	0.98	0.88	0.86	0.85	0.65	0.82
S ₆	6 th	0.98	1.14	0.60	0.60	0.59	0.60
S _{M-K}	2 nd	0.36	0.30	0.28	0.26	0.26	0.24
	4 th	0.46	0.39	0.38	0.37	0.38	0.36
	6 th	0.80	0.72	0.71	0.70	0.71	0.70
S _{M-N}	2 nd	0.38	0.29	0.26	0.26	0.30	0.26
	4 th	0.43	0.32	0.30	0.30	0.32	0.30
	6 th	0.74	0.63	0.60	0.60	0.60	0.59